Thermal Science and Engineering Progress 47 (2024) 102340

Contents lists available at ScienceDirect

Thermal Science and Engineering Progress

journal homepage: www.elsevier.com/locate/tsep

The appearance of oscillatory flows within a horizontal packed bed partly heated from below

Gazy F. Al-Sumaily [a,b,*], Hasanen M. Hussen [c], Hayder A. Dhahad [c], Mark C. Thompson [a], Talal Yusaf [d]

[a] Department of Mechanical and Aerospace Engineering, Monash University, Clayton VIC 3800, Australia
[b] Energy and Renewable Energies Technology Centre, University of Technology, Iraq
[c] Mechanical Engineering Department, University of Technology, Iraq
[d] School of Engineering and Technology, Central Queensland University, Brisbane, QLD 4009, Australia

ARTICLE INFO

Keywords:
Laminar flow
Porous media
Mixed convection
Oscillatory flows
Channel flow

ABSTRACT

We report on a numerical investigation of the unsteady mixed convective flow in a channel through a horizontal porous layer under localised isothermal heating from below to probe the oscillatory flow and thermal characteristics. The study was carried out for water flow within a plane channel containing stainless steel spherical particles. For this study, the channel height/particle diameter ratio was $H/d = 100$ and the porosity was $\varepsilon = 0.35$. The effects of the imposed pressure-driven flow characterised by the Péclet number ($0.1 \leq \mathrm{Pe} \leq 1000$), and heating represented by the Rayleigh number ($10^5 \leq \mathrm{Ra} \leq 2\times10^7$), are investigated. The results reveal that for low Péclet numbers, steady free convective flows are dominant, while for high Péclet numbers, steady forced convective flows dominate. Importantly, no oscillatory flows are found to develop in the free and forced convection regimes. However, for moderate Péclet numbers, oscillatory mixed convective flows occur with different periodic, quasi-periodic, and chaotic flow behaviours. In addition, for low Rayleigh numbers, $\mathrm{Ra} \leq 10^6$, the Nusselt number is not influenced by the Péclet number for $\mathrm{Pe} \leq 1$. Nevertheless, for high Rayleigh numbers, $\mathrm{Ra} \geq 2\times10^6$, it is observed that there always exists a critical Péclet number for which the Nusselt number is a minimum. The effects of the Péclet and Rayleigh numbers on the local and average temperature disparity between the fluid and solid phases are then investigated.

1. Introduction

Mixed convective flows in porous channels have relevance to many heat-transfer applications including cooling of electronic devices, heat sinks of micro-electronics, compact heat exchangers, and solar plants. Because of this, this topic has received considerable attention by many researchers in the past, see (Gazy et al. [1]). For example, within vertical channels, Hadim and Chen [2] examined the impact of two heating boundary conditions, namely: uniform temperature; and uniform heat flux, on the flow and heat transport. They found that a uniform temperature boundary condition has a stronger effect on heat transfer augmentation. Chen et al. [3] studied mixed convection for coupled buoyancy-aided and buoyancy-opposed pressure-driven flows in a upright porous plane channel. They reported that the most significant effect on heat transfer comes from varying the Darcy number, which characterises the porous permeability. Rami et al. [4] investigated the behaviour of mixed convection flows of a Newtonian fluid in an upright channel under constant wall temperature and solute concentration. Their results indicated that the mixed convection parameter plays a significant role in determining heat transfer rates. Degan and Vasseur [5] investigated ascending aided mixed convection flows throughout a duct employing different momentum models, in particular, the Brinkman–Darcy model and the simple Darcy model. It was found that for small values of porosity, both models produced similar results. Pop et al. [6] examined the convective flow behaviour within a narrow porous channel, noting that small values of channel width have a considerable impact on the generation of flow recirculation. Umavathi et al. [7] investigated mixed convective flows inside a standing channel for three symmetric and asymmetric wall boundary conditions, namely: isoflux–isothermal; isothermal–isoflux; and isothermal–isothermal, employing the Forchheimer–Brinkman–Darcy formulation. They reported that the Forchheimer drag coefficient is the most significant parameter that impacts the flow behaviour, particularly for the asymmetric wall

* Corresponding author at: Department of Mechanical and Aerospace Engineering, Monash University, Clayton VIC 3800, Australia.
E-mail addresses: gazy.alsumaily@monash.edu (G.F. Al-Sumaily), hasanen.m.hussen@uotechnology.edu.iq (H.M. Hussen), hayder.a.dhahad@uotechnology.edu.iq (H.A. Dhahad), mark.thompson@monash.edu (M.C. Thompson), t.yusaf@cqu.edu.au (T. Yusaf).

https://doi.org/10.1016/j.tsep.2023.102340
Received 22 July 2023; Received in revised form 12 December 2023; Accepted 15 December 2023
Available online 19 December 2023

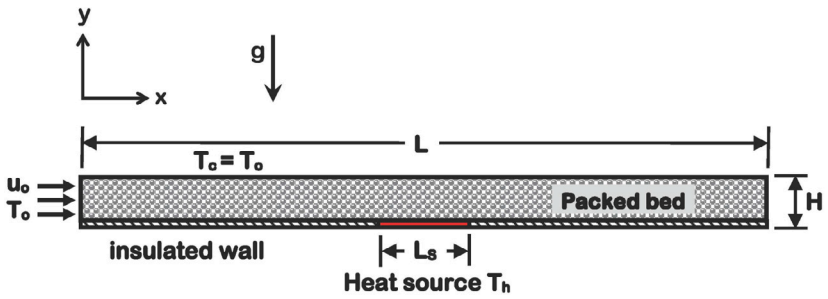

Fig. 1. Physical setup of the flow problem.

Fig. 2. Principal computational grid generated throughout the channel space.

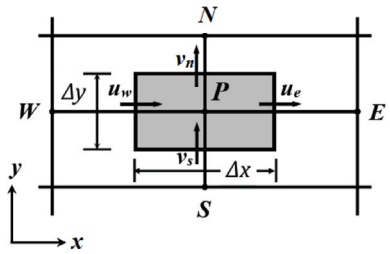

Fig. 3. Standard control volume enveloping a principal grid node P, displaying the staggered positions.

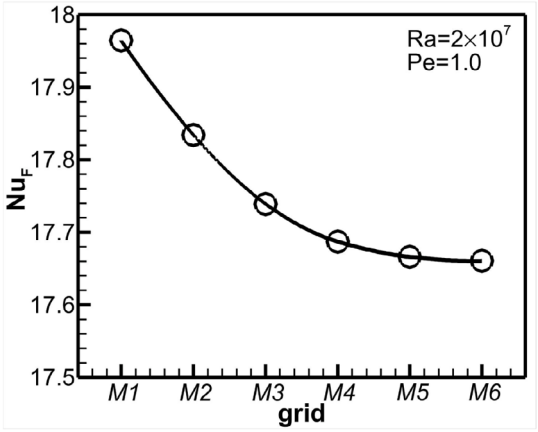

Fig. 4. Results of grid reliance study in terms of average Nusselt number, at $Ra = 2\times10^7$ and $Pe = 1.0$.

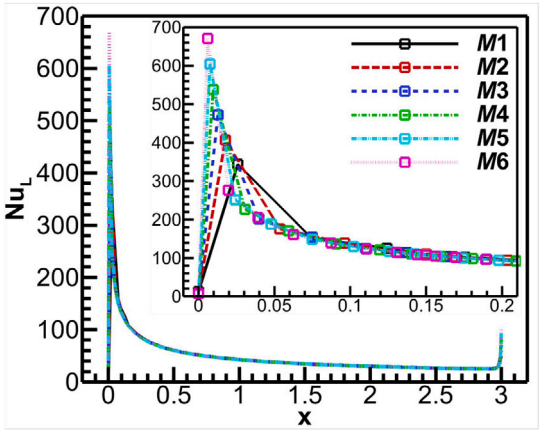

Fig. 5. Results of grid reliance study in terms of local Nusselt number, at $Ra = 2\times10^7$ and $Pe = 1000$.

boundary condition. It was pointed out that as this parameter is decreased, flow circulation occurs in the vicinity of the walls. Buonomo et al. [8] studied a time-dependent convective air flow through a vertical porous duct containing high-porosity aluminium foam, considering the assumption of thermal non-equilibrium within the porous duct. An aim was to find unsteady flow behaviour; however, the results showed that all the numerical flow solutions were steady without any indication of flow instabilities. Avramenko et al. [9] investigated convective flows inside a perpendicular round porous micro-channel under a slip boundary condition. The results showed that both the hydraulic resistance and the rate of heat removal increased with decreasing Darcy number.

Beyond those studies, mixed convection in horizontal porous channels has been also studied by many researchers. Lai et al. [13] investigated the effect of changing the size of a limited heating element placed on the bottom channel wall of a porous channel, on the thermal and hydrodynamic behaviours. They found that the heat source length does not affect the flow and temperature characteristics at low Rayleigh numbers. Nevertheless, increasing Rayleigh number generates recirculating vortices, and by increasing Péclet number, the multi-cellular flow translates to a bi-cellular one. Prasad et al. [14] analysed convective flows through a horizontal porous duct for a fixed length of heat source, which was assumed to be equivalent to the porous layer height, for various Péclet and Rayleigh numbers. Their results indicated that the conflict between the external supplied flow and the buoyant flow produces bi-cellular recirculating cells close to the heat source. Lai and Kulacki [15] investigated time-dependent convective flows within a porous channel confined by double horizontal impermeable boundaries partly warmed from below by a local heat source. The results showed tremendous oscillations in the flow behaviour and the temperature field, especially at large values of Péclet and Rayleigh numbers. They reported that using a steady-state formulation to analyse such problems provides an inadequate solution because the flow is likely to be time-dependent. Accordingly, it was recommended employing time-dependent formulations for analysing such phenomenon. Chou and Chung [16] investigated convective flows in a packed bed of spheres subjected either to constant circumferential wall temperature or constant axial heat flux. Three packed beds, namely: water–glass, air–glass, water–stainless steel particle beds, were considered. It was found that the buoyancy forces have the most crucial influence on the thermal and flow peculiarities at low thermal conductivity ratio and/or low Péclet number. However, this influence reduces considerably as

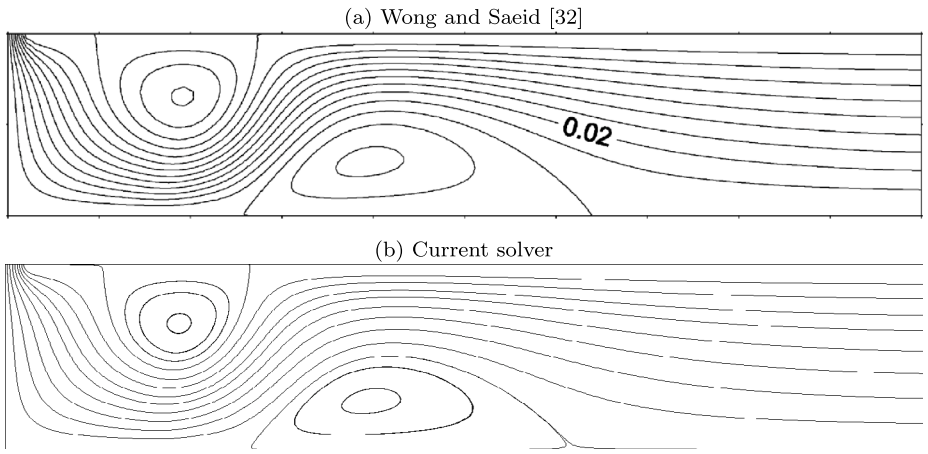

Fig. 6. Comparison between the results of (a) Wong and Saeid [10] and (b) current solver, for streamline patterns of an air jet impingement cooling of a source of heating inside a porous canal at Pe = 40.

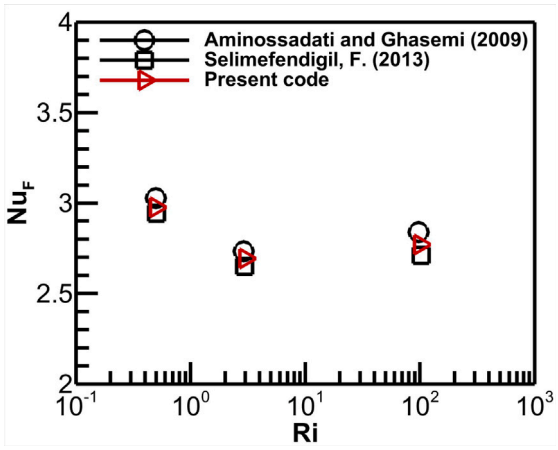

Fig. 7. Comparison amongst the results of Aminossadati and Ghasemib [11], Selimefendigil [12], and the present solver for mixed convection heat transfer from a discrete heater installed inside an open cavity within a horizontal plate channel.

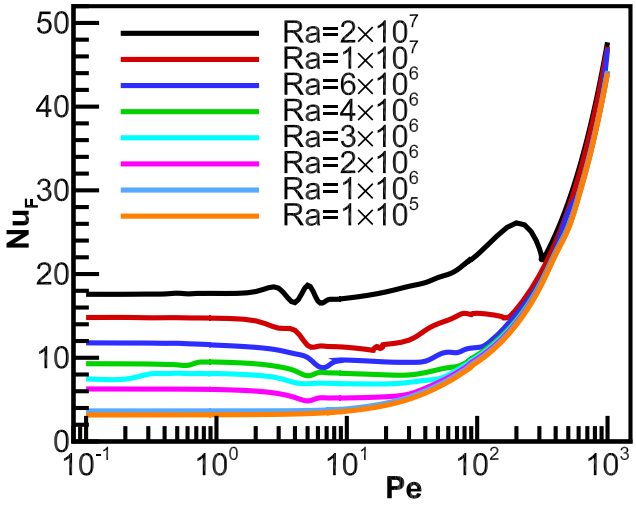

Fig. 8. Variations of Nu_F with Pe for different Ra.

either Péclet number or conductivity ratio is increased. Yokoyama et al. [17] studied convective water flows inside a channel having an abrupt expanding step, and filled with glass spheres, with heating from the bottom at the adjacent position to the step. They reported that the presence of such a step does not impact heat transfer rates. Chang et al. [18] investigated mixed convective flows in a 3-D horizontal conduit packed with stainless steel particles subject to a constant heat flux boundary condition from the right surface. They showed that increasing the Rayleigh number and decreasing the Péclet number lead to the development of secondary flows owing to the increased dominance of buoyancy forces, and then the rate of heat removal becomes higher. Cimpean et al. [19] examined analytically steady mixed convective flow within a porous inclined channel warmed by a uniform heat flux from both upper and lower surfaces. It was indicated that an increase in Péclet number reduces the impact of channel inclination on the flow and temperature distributions, and produces more symmetrical solutions. Saeid and Pop [20] studied transient convective flow in a flat porous plane channel subject to a uniform heat flux from the lower wall by a local heating element. They tested the effect of the heater length with varying the Péclet number. They observed that at moderate Péclet numbers, the convective flow begins to oscillate whenever the mixed convection mode begins to dominate the thermal system because of the conflict between buoyancy-induced effects associated with the heat source and the external flow forcing in the channel. Wong and Saeid [21] studied mixed convection forced by a heater installed on the lower surface of a horizontal channel and cooled by a jet impingement of air. They examined the impacts of the porosity and the inertial coefficient, and found that these effects become insignificant in the Darcy regime; although, in the non-Darcy regime, they turn out to be influential only once forced convection prevails. Dixon and Kulacki [22] conducted an experimental study to measure the convective heat transfer coefficient in a channel packed with glass beads, and heated at the lower surface with a finite-sized heat source. They developed an experimental correlation for Nusselt number based on the bed thickness, Rayleigh–Darcy number, and Péclet number, in an endeavour to support their previous computational results reported in Dixon and Kulacki [23]. Both the experimental and numerical results showed that the Nusselt number decreases to a minimal value at a critical Péclet number at the commencement of the mixed convection regime. Ozgen and Yasin [24] studied convective flows inside a horizontal conduit subject to heating from below to examine the influence of changing the heat source position for different Péclet and Rayleigh numbers. Their results displayed that as buoyancy effects are increased, complicated secondary cells are generated, leading to a considerable augmentation in heat removal from the conduit.

The literature review reveals that time-dependent convective flow and heat transfer through a horizontal channel packed with a porous medium partially heated from below has seen limited previous research, except perhaps the studies of Lai and Kulacki [15] and Saeid

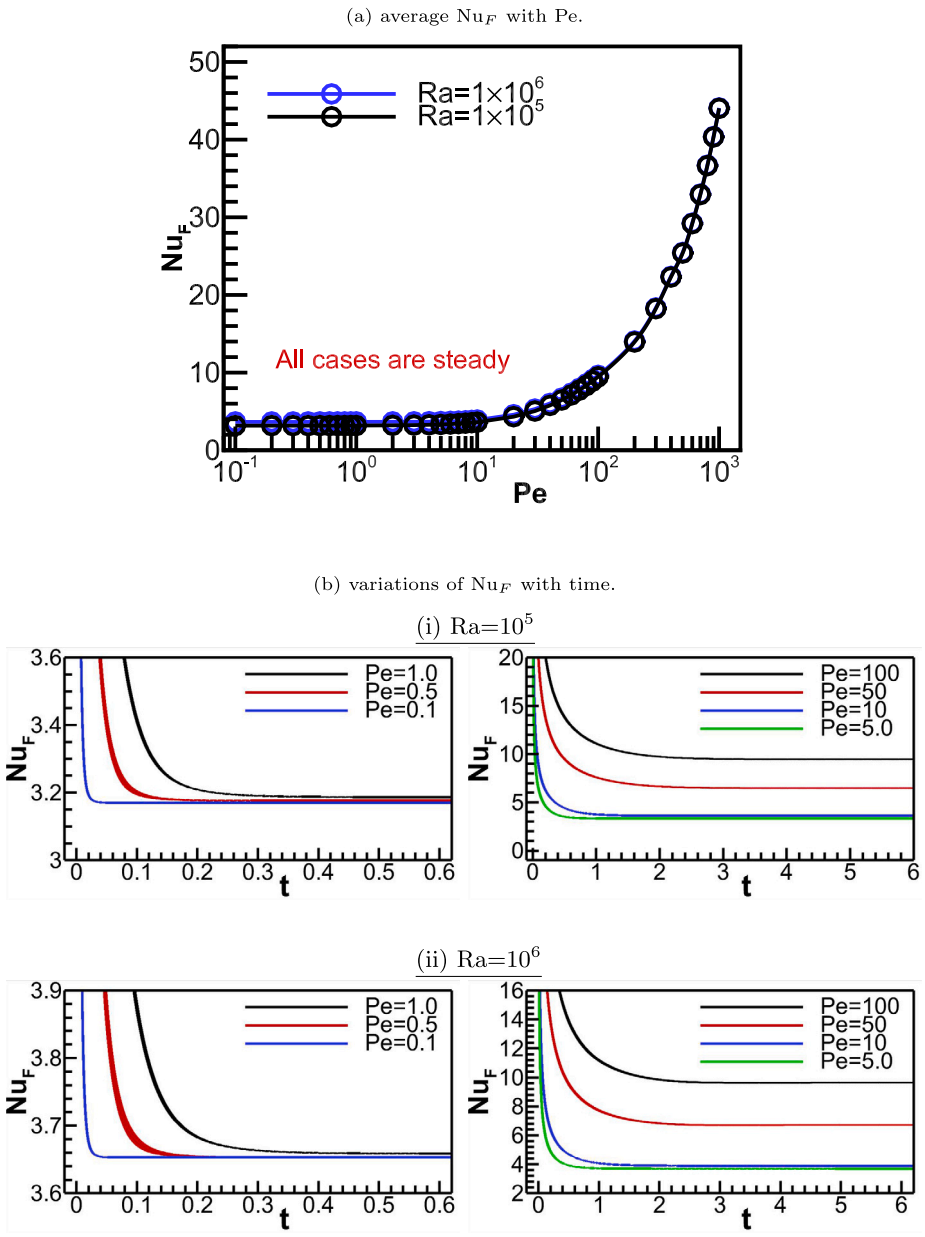

Fig. 9. (a) Variations of average Nu_F with Pe at Ra = 10^5 and 10^6, and (b) Temporal variations of Nu_F for different Pe, at (i) Ra = 10^5 and (ii) Ra = 10^6.

and Pop [20]. They discovered that convective flow begins to fluctuate at moderate Péclet numbers, hence when mixed convection starts to dominate, due to competition between buoyancy-induced forces and external pressure-driven forces. However, they did not try to identify the onset of the flow oscillation and when this oscillation vanishes. The question that can be raised here is: How does the existence of flow oscillation depend on Péclet and Rayleigh numbers? To answer this question, in the current study, we provide further analysis for the case studied previously by Lai and Kulacki [15] and Saeid and Pop [20] in an attempt to specify the critical values of Péclet number for the onset and the termination of the flow fluctuations, as the Rayleigh number is varied.

2. Mathematical formulation

The flow domain considered in the current study is a two-dimensional plane-channel of length, L, and height, H, packed with spherical particles, and heated from below using a discrete constant temperature (T_h) heating element in the middle position, as shown in Fig. 1. The channel is assumed to be sufficiently long ($L = 21H$) to be able to ignore the effects of the upstream and downstream regions on the flow behaviour in the region near the heating element. The length of the heating element is set to be the same as the channel height ($L_s = H$). In addition, water, which is taken as the working fluid, flows through the channel from the left inlet at a constant horizontal velocity (u_o) and (cold) temperature (T_o), and leaves the channel freely at the right outlet. The upper horizontal wall is isothermally cooled at a constant temperature (T_c), which is taken as the same as the inflow temperature (T_o), whereas the lower wall is insulated, except for the discrete heating element.

For the current study, the fluid flow is taken to be two-dimensional, unsteady, laminar and incompressible, and all the fluid thermo-physical properties are assumed invariant except the variation in the water density with temperature, inducing buoyancy forces through the Boussinesq approximation. Accordingly, the fluid velocities can be calculated based on the Forchheimer–Brinkman–Darcy model that incorporates the influences of inertia and viscous forces. The temperature field is calculated on the basis of the two-equation energy model, namely, the

(a) average Nu_F with Pe.

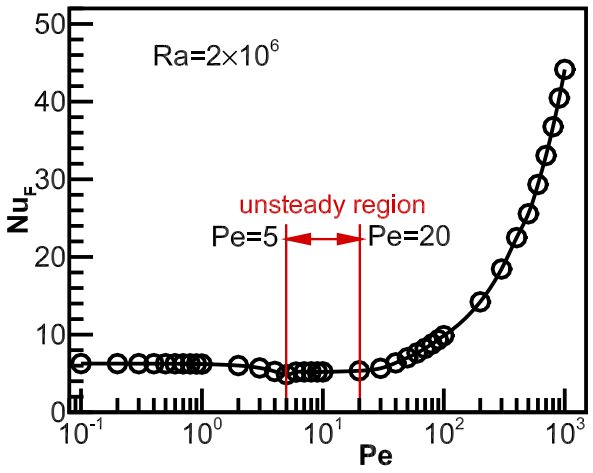

(b) variations of Nu_F with time for different Pe.

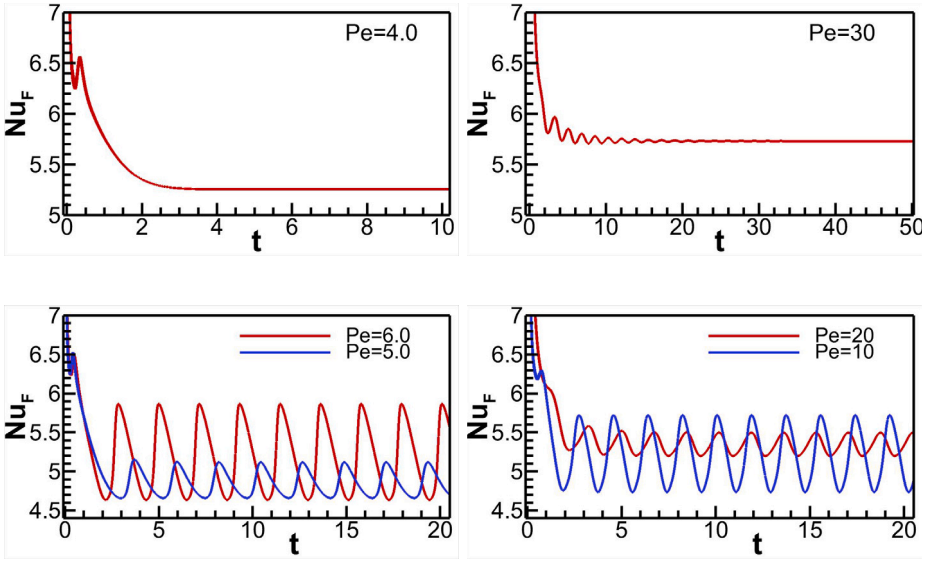

Fig. 10. (a) Variations of average Nu_F with Pe at $Ra = 2\times10^6$, and (b) Temporal variations of Nu_F for different Pe, at $Ra = 2\times10^6$.

Local Thermal Non-Equilibrium (LTNE) model, that takes into account the interfacial convection between the solid particles and the flowing fluid, so that the phases are not necessarily in thermal equilibrium. Therefore, following Kaviany [25], Nield and Bejan [26] and Mohammed et al. [27], the problem can be mathematically formulated through the following dimensional equations:

$$\nabla\cdot\langle\tilde{\mathbf{u}}\rangle = 0, \tag{1}$$

$$\frac{\rho_f}{\varepsilon}\left(\frac{\partial\langle\tilde{\mathbf{u}}\rangle}{\partial\tilde{t}} + \frac{1}{\varepsilon}\langle(\tilde{\mathbf{u}}\cdot\nabla)\tilde{\mathbf{u}}\rangle\right) = \frac{\mu_f}{\varepsilon}\nabla^2\langle\tilde{\mathbf{u}}\rangle - \nabla\langle\tilde{P}_f\rangle + \tilde{S}_{(u,v)}, \tag{2}$$

where

$$\tilde{S}_{(u)} = -\frac{\mu_f}{K}\langle\tilde{\mathbf{u}}\rangle - \frac{\rho_f C_F}{\sqrt{K}}\left|\langle\tilde{\mathbf{u}}\rangle\right|\langle\tilde{\mathbf{u}}\rangle,$$

and

$$\tilde{S}_{(v)} = -\frac{\mu_f}{K}\langle\tilde{\mathbf{u}}\rangle - \frac{\rho_f C_F}{\sqrt{K}}\left|\langle\tilde{\mathbf{u}}\rangle\right|\langle\tilde{\mathbf{u}}\rangle + \rho_f\beta g\left(\langle\tilde{T}_f\rangle - T_o\right).$$

Here

$$\left|\langle\tilde{\mathbf{u}}\rangle\right| = \sqrt{\tilde{u}^2+\tilde{v}^2}.$$

The energy equations for the fluid and solid phases are expressed as

$$\varepsilon\left(\rho c_p\right)_f\left(\frac{\partial\langle\tilde{T}_f\rangle}{\partial\tilde{t}} + \langle\tilde{\mathbf{u}}\rangle\cdot\nabla\langle\tilde{T}_f\rangle\right) = \nabla\cdot\left(k_{f.\mathrm{eff},(x,y)}\nabla\langle\tilde{T}_f\rangle\right) + h_{sf}a_{sf}\left(\langle\tilde{T}_s\rangle - \langle\tilde{T}_f\rangle\right), \tag{3}$$

$$\left(1-\varepsilon\right)\left(\rho c_p\right)_s\frac{\partial\langle\tilde{T}_s\rangle}{\partial\tilde{t}} = \nabla\cdot\left(k_{s.\mathrm{eff}}\nabla\langle\tilde{T}_s\rangle\right) - h_{sf}a_{sf}\left(\langle\tilde{T}_s\rangle - \langle\tilde{T}_f\rangle\right). \tag{4}$$

In these equations, $\langle\ldots\rangle$ is an operator denoting to the local volume average of quantities. For the case here, these are the dimensional velocity vector ($\tilde{\mathbf{u}}$), dimensional pressure ($\tilde{P}_f$) and dimensional temperature ($\tilde{T}$). Also, ε, K, C_F, h_{sf}), and a_{sf} are the porosity, permeability, inertia coefficient, interphase convective coefficient, and interphase specific superficial area, respectively. Additionally, $\tilde{S}_{(u)}$ and $\tilde{S}_{(v)}$ represent source terms in the dimensional momentum formulations, in the $\tilde{x}$- and $\tilde{y}$-directions, respectively. Finally, μ, ρ, k, β, and c_p represent the viscosity, density, thermal conductivity, thermal expansion coefficient, and specific heat capacity, respectively. The index (f) indicates the fluid phase, and the index (s) indicates the solid phase, whereas the index (eff) denotes an *effective* quantity.

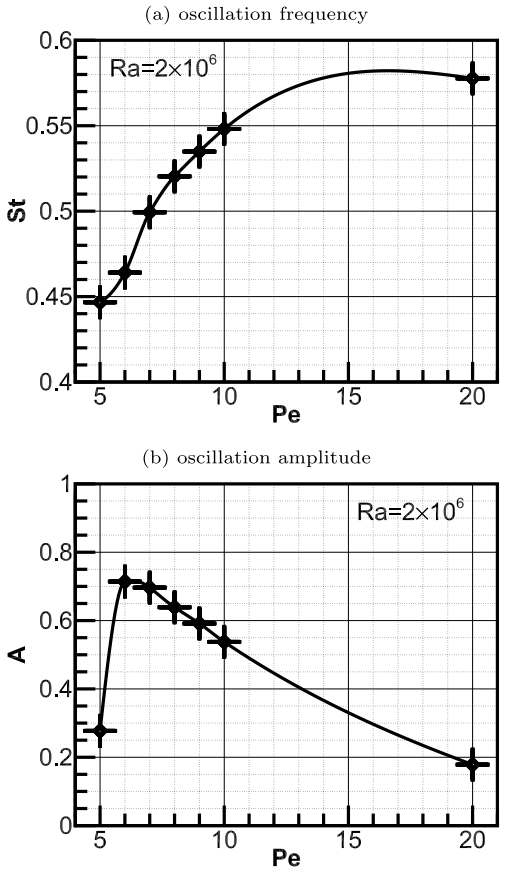

Fig. 11. Variations of (a) Strouhal number, and (b) oscillation amplitude, with Pe, at $\mathrm{Ra} = 2 \times 10^6$.

Based on the following non-dimensionalisation

$$x, y = \frac{\tilde{x}, \tilde{y}}{H}, \quad \langle \mathbf{u} \rangle = \frac{\langle \tilde{\mathbf{u}} \rangle}{u_o}, \quad t = \frac{\tilde{t} u_o}{H}, \quad \langle T_{(s,f)} \rangle = \frac{\left(\langle \tilde{T_{(s,f)}} \rangle - T_o\right)}{\left(T_h - T_o\right)}, \quad \langle P_f \rangle = \frac{\langle \tilde{P_f} \rangle}{\rho_f u_o^2}, \tag{5}$$

the non-dimensional governing equations reduce to:

$$\nabla \cdot \langle \mathbf{u} \rangle = 0, \tag{6}$$

$$\frac{\partial \langle \mathbf{u} \rangle}{\partial t} + \frac{1}{\varepsilon}\left(\langle \mathbf{u} \rangle \cdot \nabla \langle \mathbf{u} \rangle\right) = \frac{\mathrm{Pr}}{\mathrm{Pe}} \nabla^2 \langle \mathbf{u} \rangle - \varepsilon \nabla \langle P_f \rangle + S_{(u,v)}, \tag{7}$$

where

$$S_{(u)} = -\frac{\varepsilon\ \mathrm{Pr}}{\mathrm{Pe\ Da}} \langle \mathbf{u} \rangle - \frac{\varepsilon^2\ C_F}{\sqrt{\mathrm{Da}}} \left| \langle \mathbf{u} \rangle \right| \langle \mathbf{u} \rangle,$$

$$S_{(v)} = -\frac{\varepsilon\ \mathrm{Pr}}{\mathrm{Pe\ Da}} \langle \mathbf{u} \rangle - \frac{\varepsilon^2\ C_F}{\sqrt{\mathrm{Da}}} \left| \langle \mathbf{u} \rangle \right| \langle \mathbf{u} \rangle + \frac{\varepsilon\ \mathrm{Ra\ Pr}}{\mathrm{Pe}^2} \langle T_f \rangle,$$

and

$$\left| \langle \mathbf{u} \rangle \right| = \sqrt{u^2 + v^2},$$

$$\frac{\partial \langle T_f \rangle}{\partial t} + \left(\langle \mathbf{u} \rangle \cdot \nabla \langle T_f \rangle\right) = \frac{1}{\varepsilon \mathrm{Pe}} \nabla \cdot \left(\frac{k_{f.\mathrm{eff},(x,y)}}{k_f} \nabla \langle T_f \rangle \right) + \frac{\mathrm{Bi}\ k_r}{\varepsilon \mathrm{Pe}} \left(\langle T_s \rangle - \langle T_f \rangle \right), \tag{8}$$

$$\frac{\partial \langle T_s \rangle}{\partial t} = \frac{\alpha_r}{(1-\varepsilon)\ \mathrm{Pe}} \nabla \cdot \left(\frac{k_{s.\mathrm{eff}}}{k_s} \nabla \langle T_s \rangle \right) - \frac{\mathrm{Bi}\ \alpha_r}{(1-\varepsilon)\ \mathrm{Pe}} \left(\langle T_s \rangle - \langle T_f \rangle \right), \tag{9}$$

where $(\mathbf{u})$, (P_f), (T) denote to the non-dimensional flow and thermal variables, and $S_{(u)}$ and $S_{(v)}$ denote to the non-dimensional source terms. Also, α_r represents the solid/fluid thermal diffusivity ratio (α_s/α_f), while k_r represents the thermal conductivity ratio (k_s/k_f). Additionally, one can see that there are number of governing non-dimensional parameters – Rayleigh (Ra), Péclet (Pe), Darcy (Da) and Biot (Bi) numbers – emerging from the non-dimensionalisation:

$$\mathrm{Ra} = \frac{g\beta H^3 (T_h - T_c)}{\alpha_f \nu_f}, \quad \mathrm{Pe} = \mathrm{Re.Pr}, \quad \mathrm{Da} = \frac{K}{H^2}, \quad \mathrm{Bi} = \frac{H^2 h_{sf} a_{sf}}{k_s}, \tag{10}$$

where, Pr and Re are Prandtl and Reynolds numbers, as follows:

$$\mathrm{Pr} = \frac{\nu_f}{\alpha_f}, \quad \mathrm{Re} = \frac{u_o H}{\nu_f}. \tag{11}$$

The empirical expressions of Ergun [28] are employed to calculate the inertia coefficient C_F and the permeability K as follows:

$$C_F = \frac{1.75}{\sqrt{150\varepsilon^3}}, \quad K = \frac{\varepsilon^3 d^2}{150\,(1-\varepsilon)^2}. \tag{12}$$

Here, d refers to the diameter of the uniform solid particles. Additionally, the empirical expressions of Dullien [29] and Wakao et al. [30] are employed to estimate the interphase superficial specific area a_{sf} and the solid-to-fluid convective coefficient h_{sf}, respectively, as follows:

$$a_{sf} = \frac{6(1-\varepsilon)}{d}, \tag{13}$$

$$h_{sf} = \frac{k_f}{d}\left(2 + \mathrm{Pr}^{1/3}.\mathrm{Re}_p^{0.6}\right). \tag{14}$$

In this latter expression, (Re_p) is the particle Reynolds number, defined as

$$\mathrm{Re}_p = \frac{|\mathbf{u}| d}{\nu_f}. \tag{15}$$

In studying flows through packed beds numerically, the Darcy number and Biot number can be related to particle diameter and porosity. Thus, by substituting the permeability Eq. (12) into the expression for the Darcy number

$$\mathrm{Da} = \left(\frac{d}{H}\right)^2 \frac{\varepsilon^3}{150\,(1-\varepsilon)^2}, \tag{16}$$

while substituting Eqs. (13) and (14) in the Biot number definition gives

$$\mathrm{Bi} = 6\,(1-\varepsilon)\left(\frac{1}{k_r}\right)\left(\frac{H}{d}\right)^2 \left(2 + (\mathrm{Pr})^{1/3}\,(\mathrm{Re}_p)^{0.6}\right). \tag{17}$$

In the current investigation, the effective thermal conductivity of the fluid phase, $k_{f.\mathrm{eff},(x,y)}$, includes the effects of the dispersion conductivity, $k_{d,(x,y)}$, in the x- and y-directions, and the stagnant conductivity, $k_{st.f}$,

$$k_{f.\mathrm{eff},(x,y)} = k_{d,(x,y)} + k_{st.f}. \tag{18}$$

The experimental correlation of Zehner and Schluender [31] is employed to calculate $k_{st.f}$:

$$k_{st.f} = k_f. \left[\left(1 - \sqrt{1-\varepsilon}\right) + \left(\frac{2\sqrt{1-\varepsilon}}{1-\lambda B}\right)\left(\frac{(1-\lambda)B}{(1-\lambda B)^2} \ln(\lambda B) - \frac{B+1}{2} - \frac{B-1}{1-\lambda B}\right)\right], \tag{19}$$

whereas, the practical formulations of Wakao and Kaguei [32] are employed to calculate $k_{d,(x,y)}$

$$k_{d,(x)} = k_f\left(0.5\ \mathrm{Pr\ Re}_p\right), \quad k_{d,(y)} = k_f\left(0.1\ \mathrm{Pr\ Re}_p\right). \tag{20}$$

Here, $B = 1.25\left((1-\varepsilon)/\varepsilon\right)^{\frac{10}{9}}$ and $\lambda = 1/k_r$. However, the effective thermal conductivity of the solid phase ($k_{s.\mathrm{eff}}$) includes only the impact

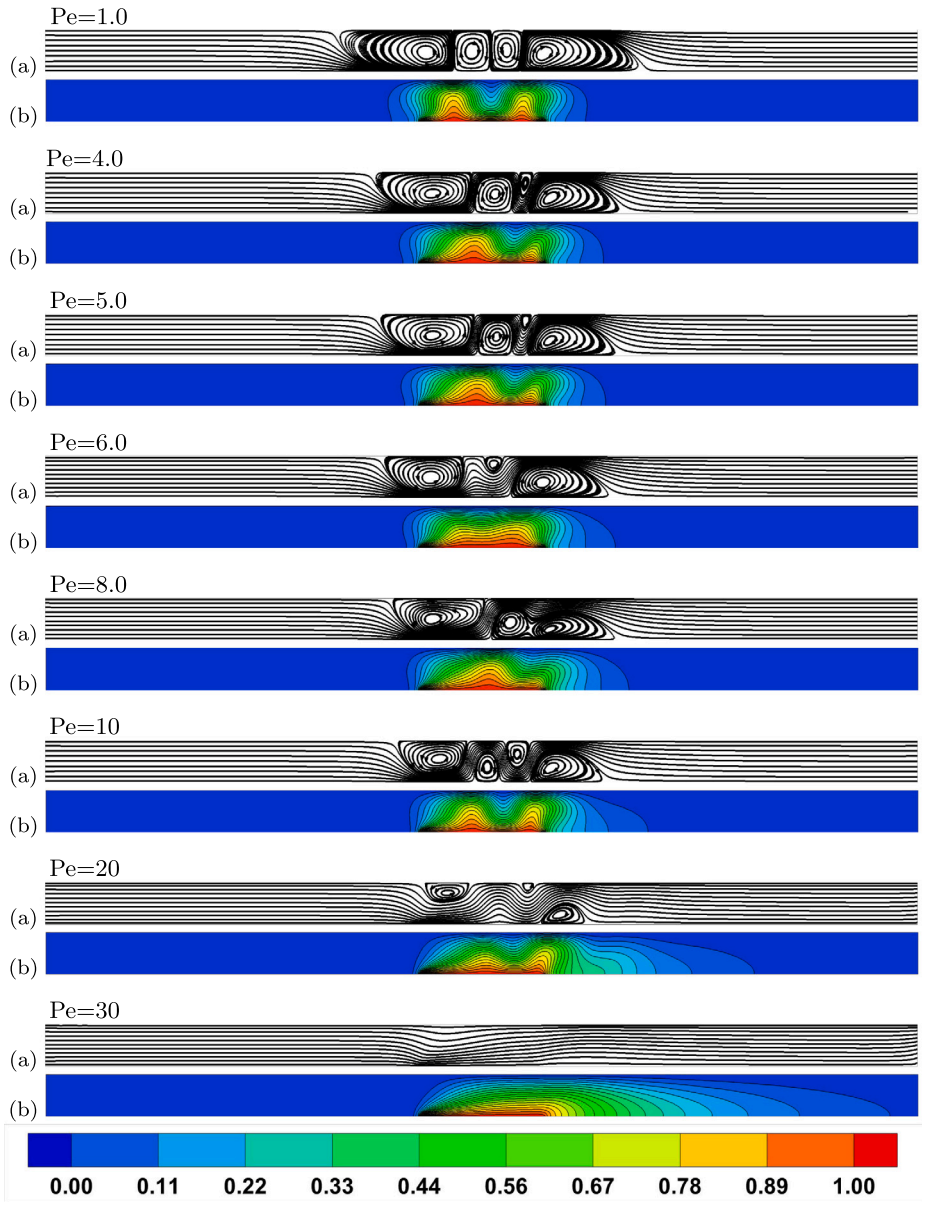

Fig. 12. (a) Streamlines patterns and (b) isotherms patterns, at different Pe and at Ra $= 2 \times 10^6$.

of the stagnant conductivity ($k_{st.s}$) in the solid spheres, which is calculated employing an another experimental correlation of Zehner and Schluender [31],

$$k_{st.s} = k_s.(1-\varepsilon). \tag{21}$$

3. Boundary conditions and heat transfer

For the velocities and the temperatures, Dirichlet boundary conditions are employed at the channel surfaces, heat source, and the inlet, whereas, Neumann boundary conditions are used at the outlet. Specifically:

Inlet: at $(x = 0)$ and $(0 < y < H)$, $u_o = 1$, and $v_o = T_o = 0$,

Upper surface: at $(y = H)$ and $(0 < x < L)$, $T_c = T_o = 0$, and $u = v = 0$,

Lower surface (except heater): at $(y = 0)$ and $(0 < x < L)$, $\dfrac{\partial T}{\partial y} = u = v = 0$,

Heater: at $(y = 0)$ and along (L_s), $T_h = 1$ and $u = v = 0$,

Outlet: at $(x = L)$ and $(0 < y < H)$, $\dfrac{\partial T}{\partial x} = \dfrac{\partial u}{\partial x} = \dfrac{\partial v}{\partial x} = 0$. (22)

The mean fluid Nusselt number (Nu_F) is estimated by integrating the local Nusselt number over the heater length,

$$\mathrm{Nu}_F = \frac{1}{L_s}\sum \int_{L_s} \left(\frac{-k_{f.\mathrm{eff}}}{k_f} \frac{\partial T_f}{\partial y} \right) dx. \tag{23}$$

4. Numerical approach

To numerically solve the differential Eqs. (6)–(9) and estimate the velocity and temperature fields in the channel, the finite-volume approach is utilised to computationally discretise the equations and incorporate boundary conditions. This approach, which is described thoroughly in Patankar [33], is incorporated in our in-house FORTRAN software to predict the development of the flow and energy transfer of the time-dependent mixed convection flow in the porous channel. Briefly, at first, the channel space is entirely split into horizontal and vertical lines generating the principal computational grid described in Fig. 2. As illustrated in Fig. 2, a non-uniform spacing is used in the zones that undergo high gradients, e.g., near the heat source and the solid boundaries. The points of intersection between the perpendicular

(a) average Nu_F with Pe.

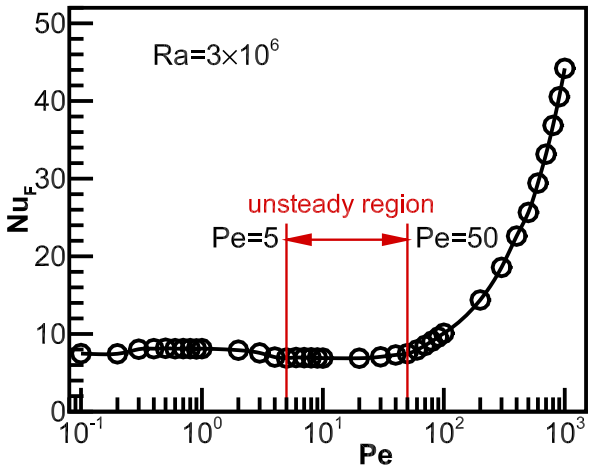

(b) variations of Nu_F with time for different Pe.

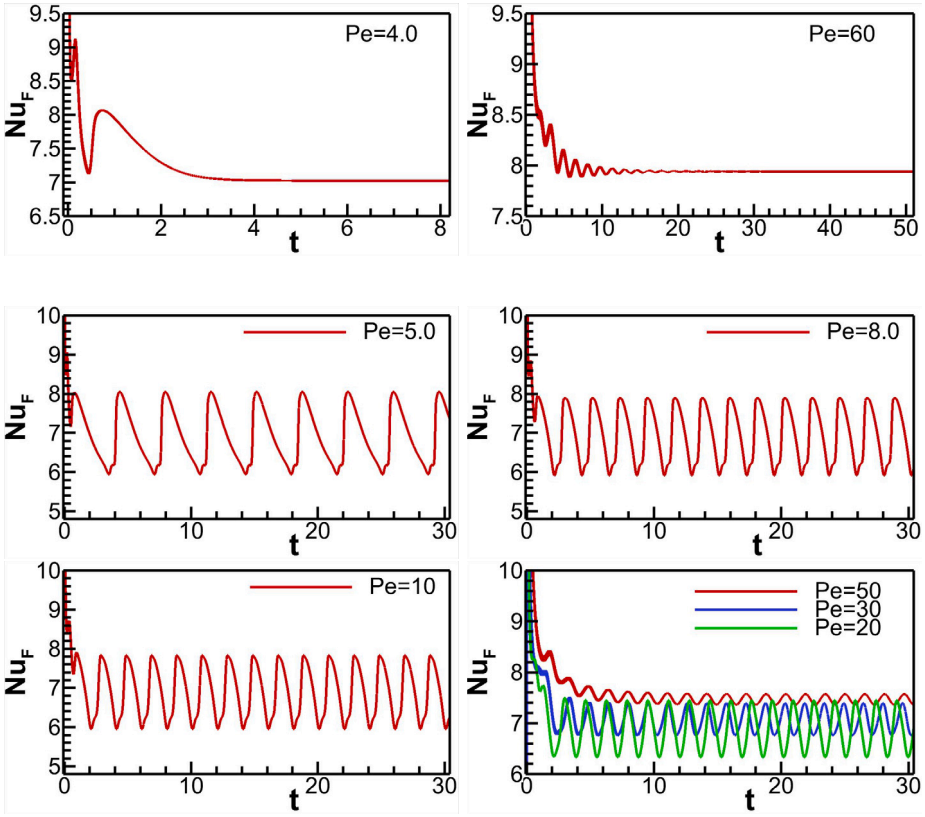

Fig. 13. (a) Variations of average Nu_F with Pe at Ra $= 3 \times 10^6$, and (b) Temporal variations of Nu_F for different Pe, at Ra $= 3 \times 10^6$.

and horizontal lines are so-called grid nodes. Every grid node (P) is enveloped by so-called a control volume, which comprises imaginary borders positioned in the halfway between the node P and any adjacent node (N), (S), (E), or (W). The positions of these imaginary borders produce a supplementary secondary computational grid known as a *staggered* grid. Fig. 3 depicts a standard control volume having dimensions ($\Delta x \times \Delta y$) enveloping a principal grid node P connecting with the four adjacent nodes N, S, E, and W, and displaying the locations of staggered grid. Typically, the pressure and temperature variables are estimated at the principal nodes, whereas the velocity field is estimated at the staggered locations. After that, the hybrid differencing scheme, reported in Ferziger and Peric [34], is employed to integrate the differential Eqs. (6)–(9) across the computational grid for producing non-linear algebraic formulations. Then, the SIMPLEC algorithm of Patankar [33] is used to link the continuity and momentum formulations, and solve them simultaneously with the energy formulation using the alternating direction implicit (ADI) approach.

A grid reliance study was conducted to assure that the results acquired from the current code are independent of computational grid. During this study, six different grid sizes namely, $M1$, $M2$, $M3$, $M4$, $M5$, and $M6$, which are detailed in Table 1, were employed. This study was performed at different Rayleigh and Péclet numbers. For instance, Fig. 4 displays the results of the variation of average fluid Nusselt number Nu_F at Ra $= 2 \times 10^7$ and Pe $= 1.0$, whereas, Fig. 5 displays

(a) average Nu_F with Pe.

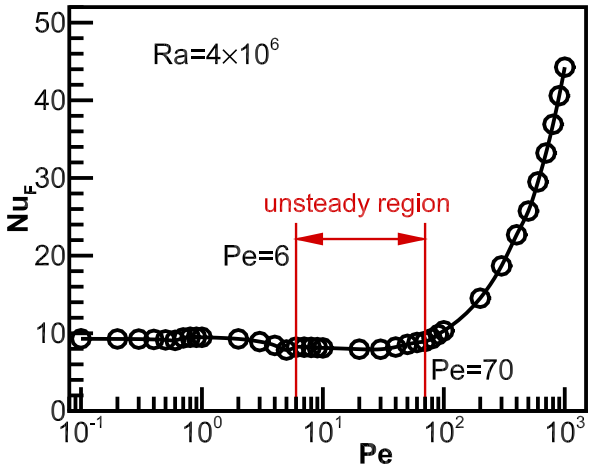

(b) variations of Nu_F with time for different Pe.

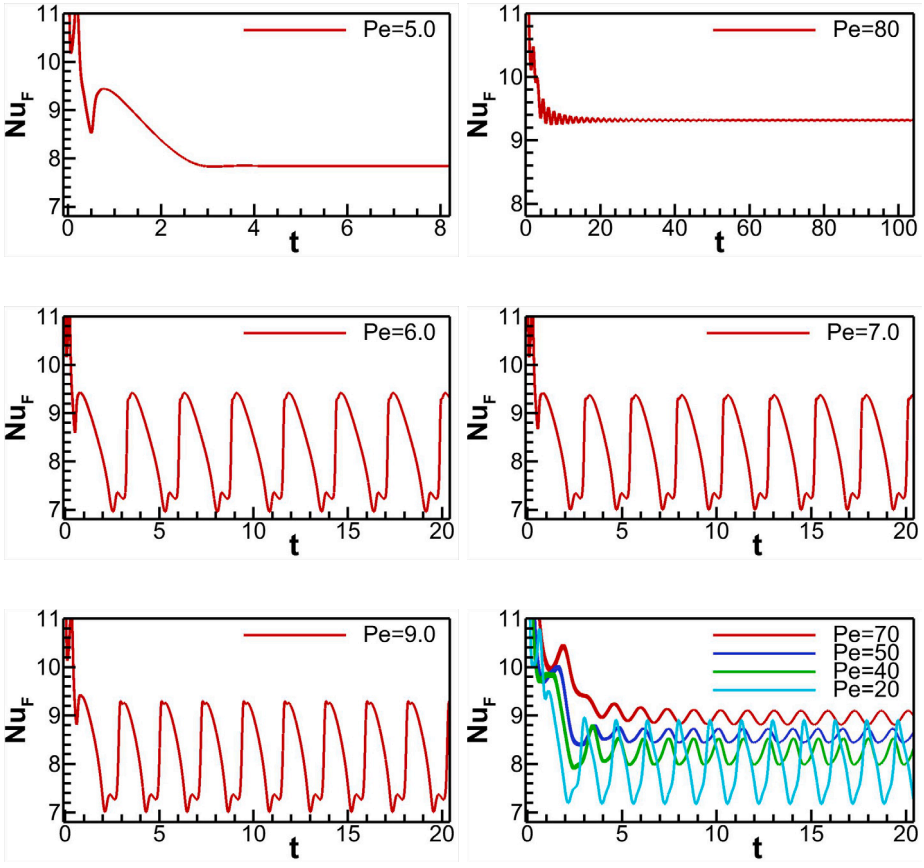

Fig. 14. (a) Variations of average Nu_F with Pe at Ra $= 4 \times 10^6$, and (b) Temporal variations of Nu_F for different Pe, at Ra $= 4 \times 10^6$.

the results in terms of local Nusselt number (Nu_L) at Ra $= 2 \times 10^7$ and Pe $= 1000$. The study revealed that the computational grid $M5$ with size of ($\Delta x \times \Delta y = 161 \times 61$) is appropriate to be used in the present investigation because it permits a rational settlement between the time and the accuracy with an utmost deviation $< 0.01\%$.

Our existing solver was validated against the numerical results of Wong and Saeid [10] for the problem of air jet impingement cooling of a source of heating inside in a porous canal. Fig. 6 demonstrates the results of both algorithms for streamline patterns at Pe $= 40$, and shows a reasonable agreement between them. It is noteworthy that we used this software in our previous works (Mohammed et al. [27], Alawee et al. [35], Hayder et al. [36]) to analyse mixed convective flows in porous channel and cavity, respectively. In addition, the numerical

Table 1
Grid sizes employed to check the grid independency.

Mesh	$M1$	$M2$	$M3$	$M4$	$M5$	$M6$
($\Delta x \times \Delta y$)	(121 × 21)	(131 × 31)	(141 × 41)	(151 × 51)	(161 × 61)	(171 × 71)

(a) average Nu_F with Pe.

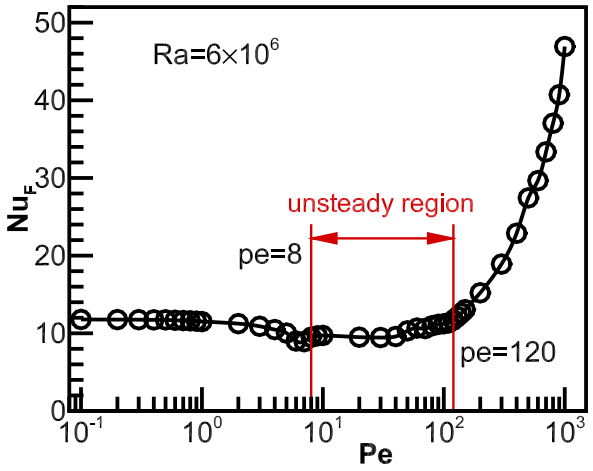

(b) variations of Nu_F with time for different Pe.

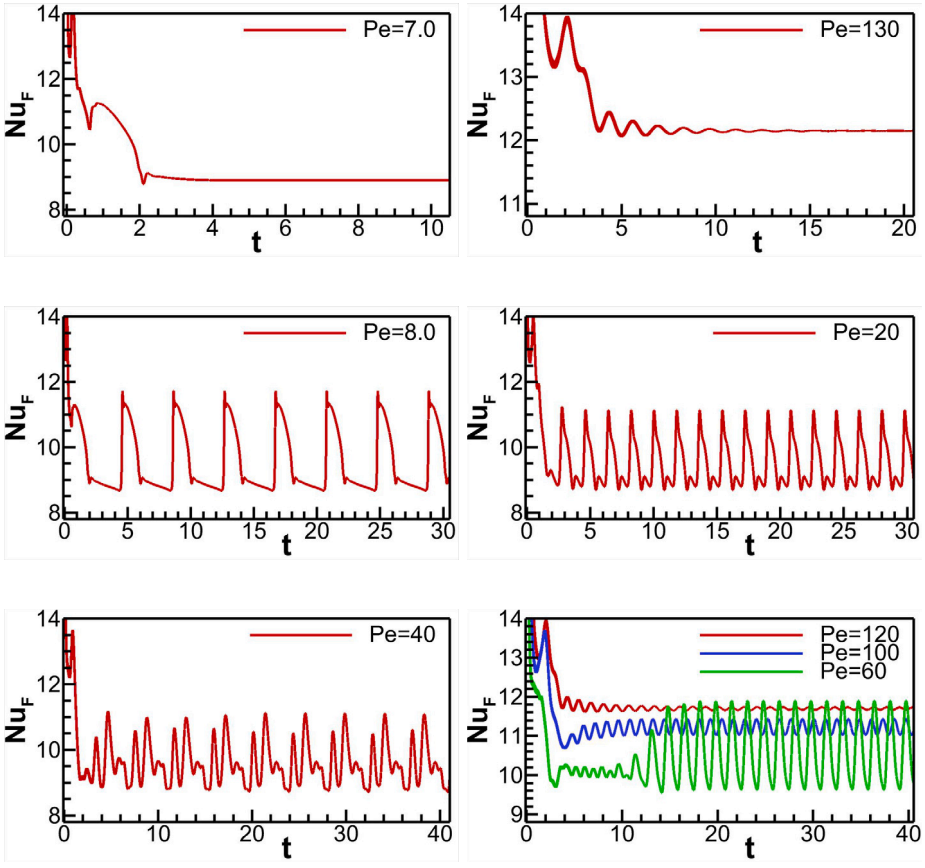

Fig. 15. (a) Variations of average Nu_F with Pe at Ra $= 6 \times 10^6$, and (b) Temporal variations of Nu_F for different Pe, at Ra $= 6 \times 10^6$.

accuracy of the solutions is characterised by means of a quantitative comparison amongst the results of Aminossadati and Ghasemib [11], Selimefendigil [12], and the present solver for mixed convection heat transfer from a discrete heater installed on the bottom of an open cavity within a horizontal plate channel (see Fig. 7).

5. Results and discussion

This investigation is performed to examine water flow through a horizontal plane channel packed with stainless steel particles, for a range of Péclet (Pe = 0.1 – 1000) and Rayleigh numbers (Ra = 10^5 – 2×10^7). The thermal and structural properties of water and stainless steel, which are illustrated in Table 2, are considered to be constant for this investigation.

The plots of mean fluid Nusselt number against Péclet number for a range of Rayleigh numbers are displayed in Fig. 8. The figure displays that the magnitude of the Nusselt number increases as the Rayleigh number is increased. However, the impact of the Rayleigh number entirely vanishes for higher values of Péclet number, Pe $\geq$ 400. In addition, it is found that for low Rayleigh numbers, Ra $\leq 10^6$, Nusselt

(a) average Nu_F with Pe.

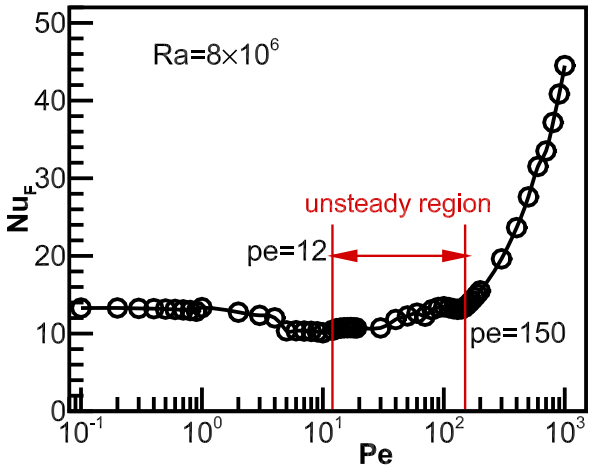

(b) variations of Nu_F with time for different Pe.

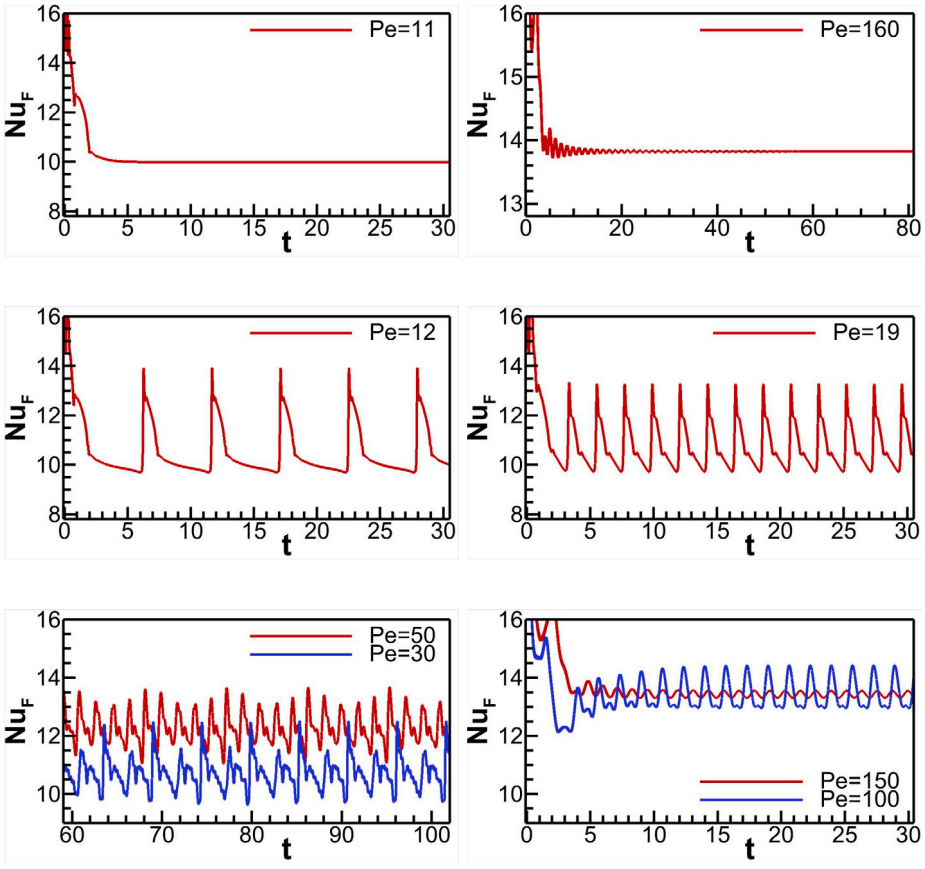

Fig. 16. (a) Variations of average Nu_F with Pe at Ra $= 8 \times 10^6$, and (b) Temporal variations of Nu_F for different Pe, at Ra $= 8 \times 10^6$.

number is unaffected by Péclet number for Pe $\leq$ 1. This is attributed to the domination of Bénard convection in the channel. However, for Pe $>$ 1, the Nusselt number is found to always increase as Péclet number is increased. Importantly, one can see that for Pe $>$ 10, the slopes of Nusselt number curves increase remarkably due to the dominance of forced convection. It is clear that the curves of Nusselt number are smooth for this low range of Rayleigh number, Ra $\leq 10^6$. Nevertheless, for higher Rayleigh numbers, Ra $\geq 2 \times 10^6$, it is observed that the curves always have minima at critical Péclet numbers. The existence of a critical Péclet number could be ascribed to the balance between the competition between forced and free convection. In particular, this critical Péclet number occurs when the augmentation in heat transfer due to the forced convection is less than the diminution from free convection. Interestingly, it is shown that the curves of Nusselt number do not change smoothly with Péclet number for almost the entire range 3 $\leq$ Pe $\leq$ 300. This is due to the existence of unsteady flow in

(a) average Nu_F with Pe.

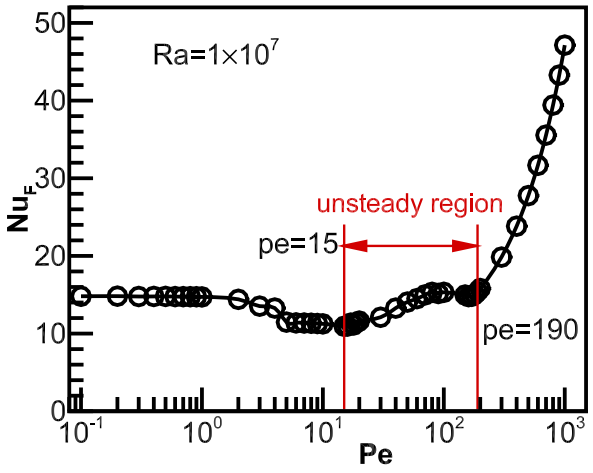

(b) variations of Nu_F with time for different Pe.

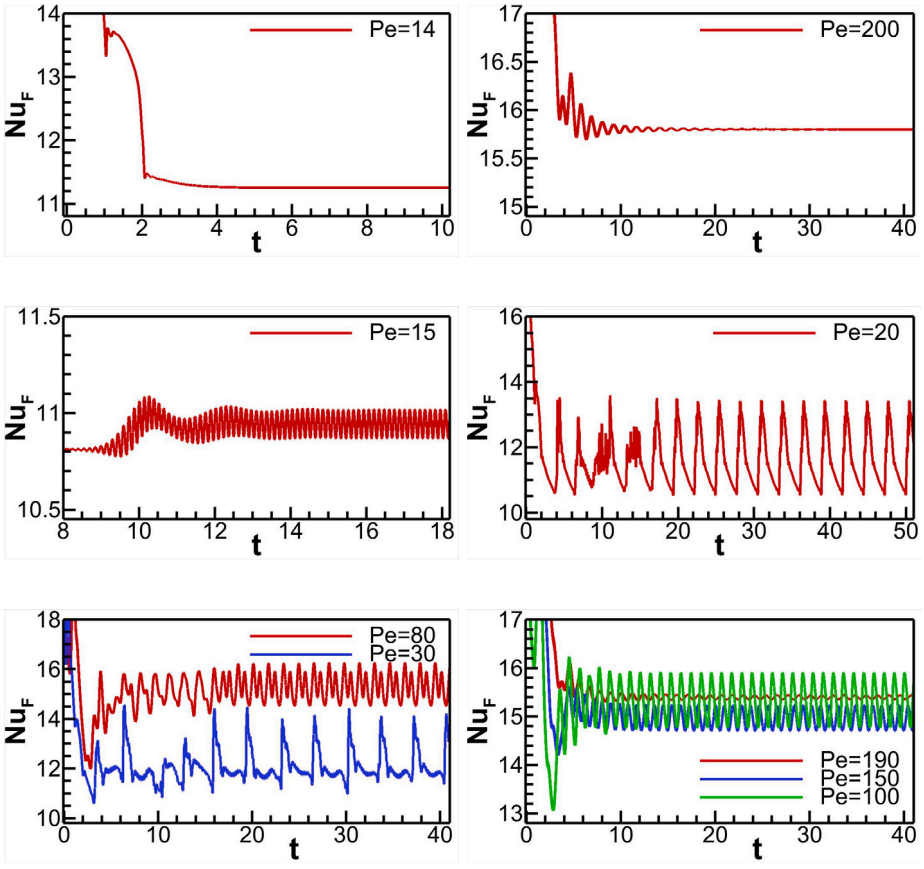

Fig. 17. (a) Variations of average Nu_F with Pe at Ra = 10^7, and (b) Temporal variations of Nu_F for different Pe, at Ra = 10^7.

the channel. Therefore, the flow behaviour needs to be investigated carefully over this Péclet number range.

To explore this further, numerical simulations were undertaken for small increments of Péclet number at each Rayleigh number. Fig. 9a shows the Nusselt number variation for two Rayleigh numbers: Ra = 10^5 and 10^6. Notably, it was found that all flow predictions reached a steady state without fluctuating with time, showing smooth variation with Péclet number. Additionally, one can see that Nusselt number is only weakly influenced by Rayleigh number, with more influence seen at moderate and higher Péclet numbers. Hence, for Pe = 0.1 – 10, the Nusselt number is effectively invariant, demonstrating the dominance of Bénard convection, while, for Pe > 10, Nusselt number increases strongly with Péclet number. This critical Péclet number denotes to the beginning of the mixed convection regime that means both convection and buoyancy effects play a role in affecting the heat transfer. Fig. 9b exhibits the variations of mean Nusselt number with time at Ra = 10^5

(a) average Nu_F with Pe.

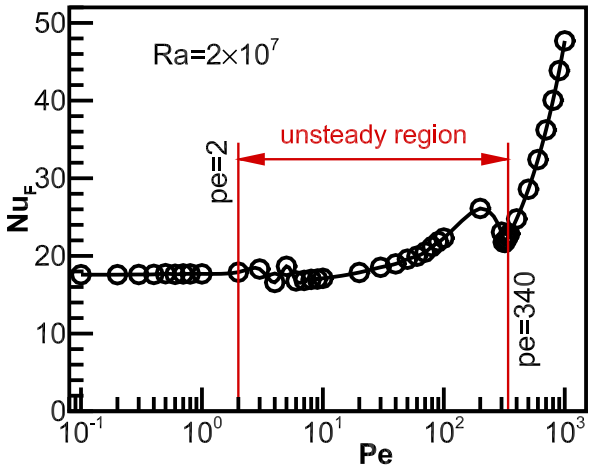

(b) variations of Nu_F with time for different Pe.

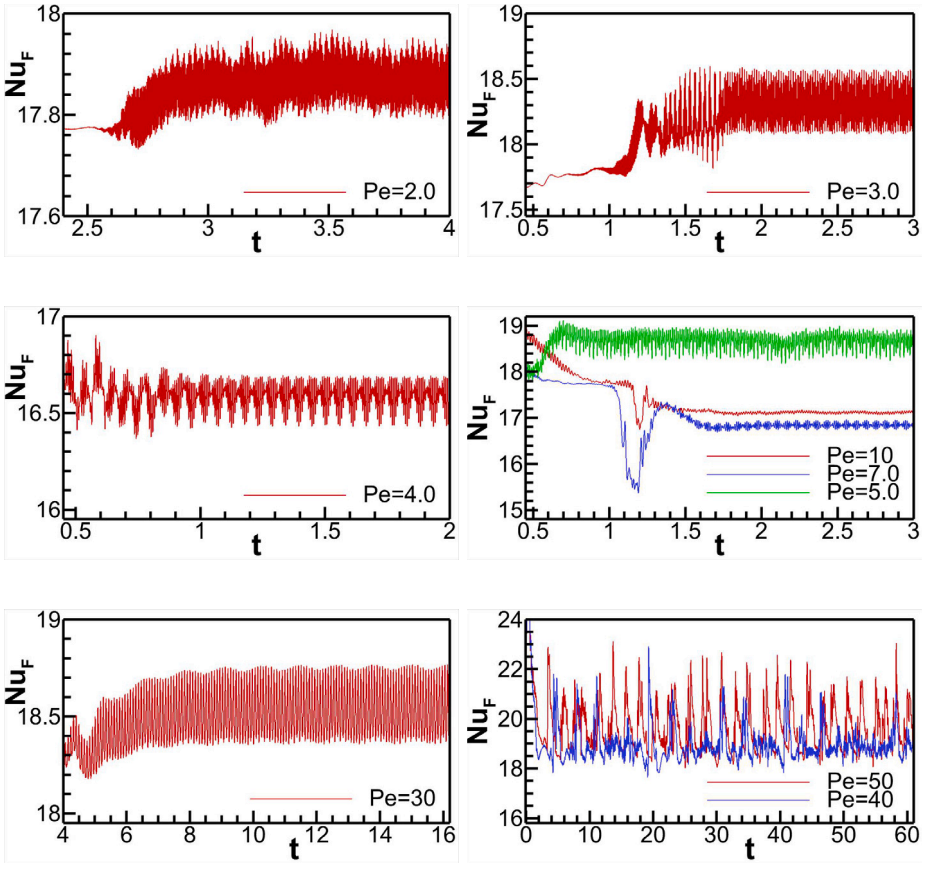

Fig. 18. (a) Variations of average Nu_F with Pe at Ra $= 2 \times 10^7$, and (b) Temporal variations of Nu_F for different Pe, at Ra $= 2 \times 10^7$.

and 10^6, and for the whole range of Péclet number. It is observed that for all cases, the Nusselt number monotonically decreases with time until reaching the steady-state asymptotic value. Another interesting finding is that the behaviour of the transient time taken for approaching steady state decreases as the Péclet number is reduced. For instance, the case of Pe = 0.1 requires the shortest time to reach the steady-state solution, as the strength of the forced flow heat transfer is very weak in comparison to straight heat conduction. This also reflects that the time scaling is based on a convective time scale rather than a thermal conduction time scale.

Next, considering the case of Ra $= 2 \times 10^6$, the temporal variations of Nusselt number at different Péclet numbers are presented in Fig. 10. It can be seen that for $0.1 \leq$ Pe ≤ 4, the flow field reaches a steady state after a transient period and becomes stable. However, for $5 \leq$ Pe ≤ 20, it is worthwhile to record that the flow field becomes unstable and oscillatory. Thus, the Nusselt number does not reach a steady

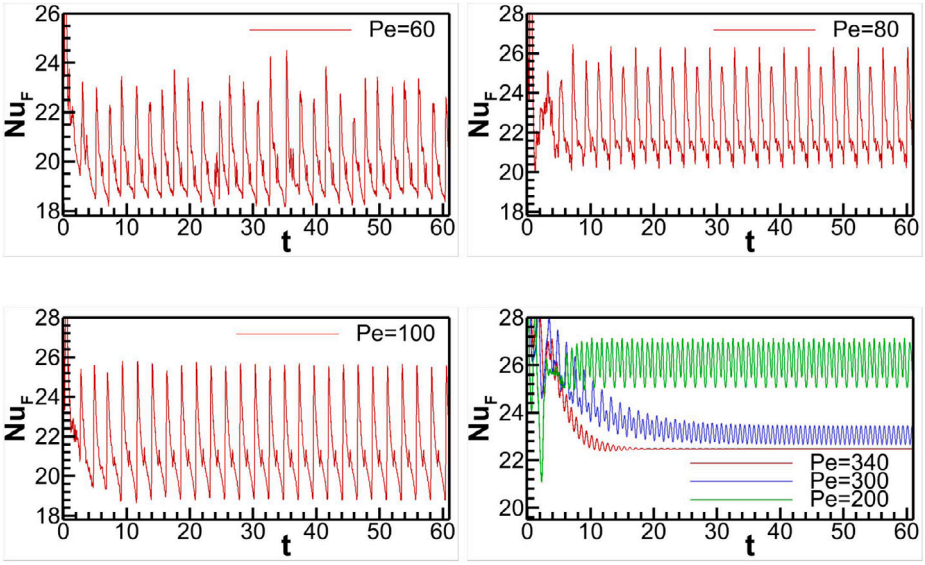

Fig. 18. (*continued*).

(a) Variation of Nu_F with time at Ra=2×10^7 and Pe=2.0.

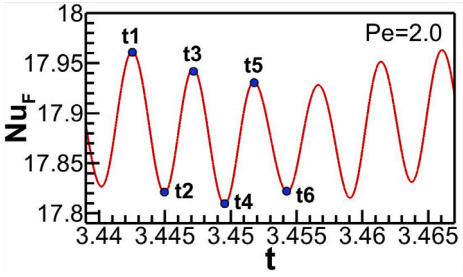

(b) Streamlines of flow.

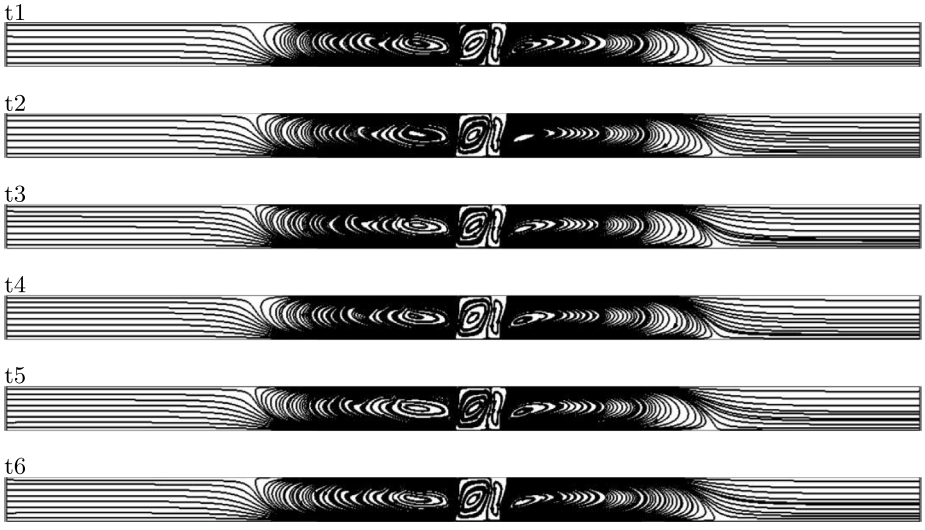

Fig. 19. (a) Variations of Nu_F with time at Ra = 2×10^7 and Pe = 2.0, and (b) streamlines of flow behaviour at different times indicated in (a).

state condition but fluctuates with time. Fig. 11, which displays the variations of Strouhal number (St) representing the frequency of flow fluctuation and the oscillation amplitude (A), against Péclet number, demonstrates that this flow fluctuation has a low frequency at Pe = 5 that increases as Péclet number is increased. Over this range, the fluctuating amplitude increases to a peak value as Péclet number is

(a) Variation of Nu_F with time at Ra=2×10^7 and Pe=4.0.

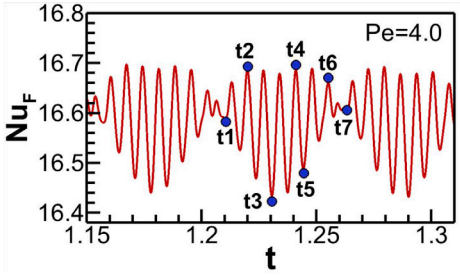

(b) Streamlines of flow.

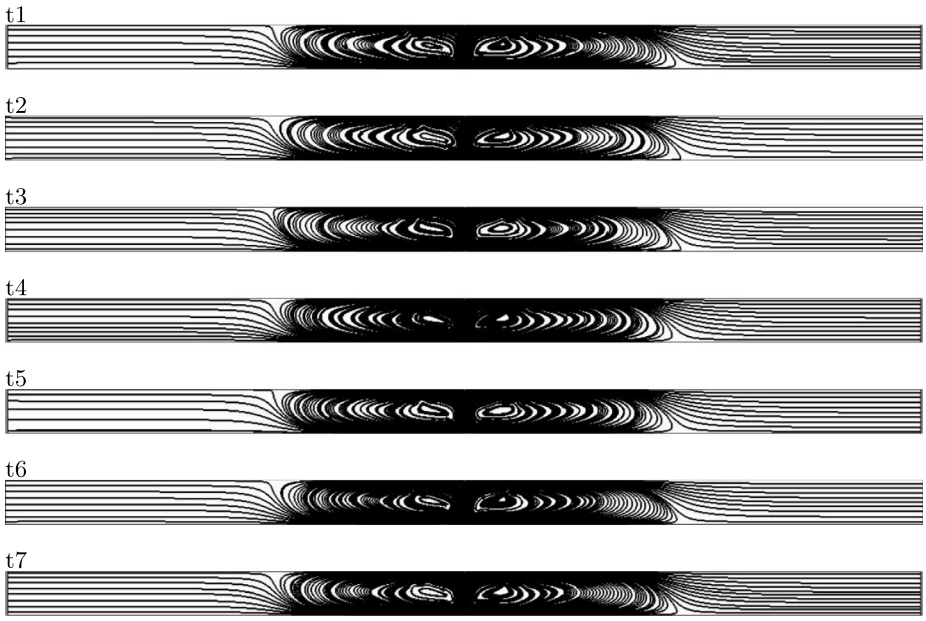

Fig. 20. (a) Variations of Nu_F with time at Ra = 2×10^7 and Pe = 4.0, and (b) streamlines of flow behaviour at different times indicated in (a).

Table 2
Thermal and structural properties of water and stainless steel considered in this study.

Water properties	
Pr	7.1
k_f (W/m K)	0.609
α_f (m^2/s)	0.14559×10^{-6}
Stainless steel properties	
k_s (W/m K)	52
α_s (m^2/s)	0.13248×10^{-4}
ϵ	0.35
H/d	100

increased from Pe = 5 to 6; however, thereafter, it decreases until reaching a small magnitude at Pe = 20. For Pe > 20, there is no fluctuation, indicating that the flow once again becomes stable.

Fig. 12 illustrates the impact of increasing flow convection, quantified by Péclet number, on the flow and the temperature distributions at Ra = 2×10^6. It is noted that for low Péclet number, Pe ≤ 1, the velocity and temperature distributions are strongly affected near the edges of the heater. Thus, multiple recirculation cells and buoyant plumes are generated along the heater length. For example, the figure demonstrates that at Pe = 1, four convective cells and two reversed plumes have developed above the heater, indicating that buoyancy is dominant. By raising the Péclet number to Pe = 4, one of the two inner cells is suppressed. For increased Péclet number, the flow is seen to change between from a strong multicellular structure spanning the entire channel height to smaller cells attached only to one wall. Eventually, at even higher Péclet number, pure forced convection dominates and all recirculation cells disappear.

It is worth mentioning that Horne and O'Sullivan [37,38] reported that oscillatory flow developed in a free convection dominated flow within a porous medium fed by disturbances generated by an instability of the thermal boundary layer. Nevertheless, in the existing investigation, no oscillatory flows are found to develop in the free-convection regime even for higher Rayleigh numbers, as we will see later. The current results show periodic flow cells occur within the mixed convection regime as a result of only the unsteadiness in the thermal boundary layer. Indeed, such flow instability takes place through the interconnection between buoyancy forces and the externally induced flow. Hence, the buoyancy forces have the predisposition to enlarge the thermal boundary layer; while the external flow forces tend to restrain it. Also, the presence of the top horizontal surface strengthens further this interconnection by assisting in the destruction and restoration of the circulating convection cells.

Now, the question is: How is the range of Péclet number for flow instability to occur affected by the amount of heating from the heat

(a) Variation of Nu_F with time at Ra=2×10^7 and Pe=40.

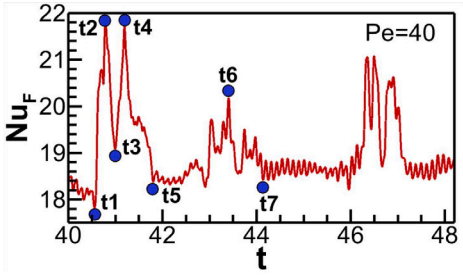

(b) Streamlines of flow.

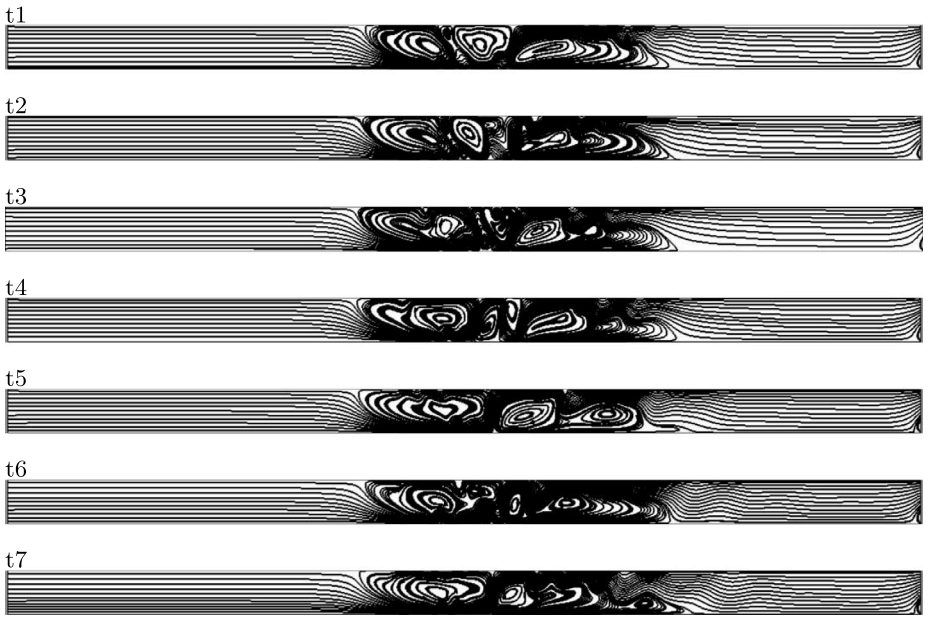

Fig. 21. (a) Variations of Nu_F with time at Ra $= 2\times10^7$ and Pe = 40, and (b) streamlines of flow behaviour at different times indicated in (a).

source represented by Rayleigh number? To answer this question, numerous numerical runs were conducted at many Rayleigh numbers. Thus, Figs. 13–18 display the detailed variations of Nusselt number against Péclet number at Ra $= (3, 4, 6, 8\times10^6), 10^7, 2\times10^7$, along with their transient responses. In Fig. 13, it is obvious that as Rayleigh number is increased from Ra $= 2\times10^6$ to Ra $= 3\times10^6$, the range of Péclet number that causes oscillation in Nusselt number increases. Thus, the onset of the flow oscillation occurs at approximately the same magnitude of Péclet number of Pe = 5, but the extent of the flow oscillation range extends to Pe = 50. Thus, the range of Péclet number leading to flow instability is increased 3 times, despite having the same lower Péclet number bound. One can observe that the oscillation period together with the oscillation amplitude are reduced as Péclet number is increased. Fig. 14 shows that as Rayleigh number is increased to Ra $= 4\times10^6$, the onset of the flow oscillation shifts slightly to begin at Pe = 6, and the termination of the flow oscillation shifts towards Pe = 70. Hence, the range of the flow instability is increased by 1.4 times as Rayleigh number is raised from Ra $= 3\times10^6$ to Ra $= 4\times10^6$. Indeed, this can be attributed to the fact that buoyancy effects increase with increasing Rayleigh number, as well as that the balance with the external-induced flow for flow oscillation requires higher Péclet number. Once again, the lower the Péclet number, the shorter the time period of oscillation and the smaller the oscillation amplitude.

In Figs. 15–17, it is shown that at Ra $= 6\times10^6$ unsteady oscillations occur over the range $8 \le$ Pe ≤ 120, which is a 1.75 times increase in the range of Péclet number, and at Ra $= 8\times10^6$ unsteady solutions occur for $12 \le$ Pe ≤ 150, which a 1.23 times increase in the range of Péclet number. Increasing Rayleigh number further to Ra $= 1\times10^7$ leads to an unstable range of $15 \le$ Pe ≤ 190, with a 1.26 times increase in the range. It is also shown that as Rayleigh number is raised, the lower and upper limits both increase, but the increase in the higher limit increasing faster than the lower limit. In addition, at high Rayleigh numbers of Ra $= 8\times10^6$ and 2×10^7, the previously observed periodic flow oscillations are observed to convert into quasi-periodic oscillations. For instance, this is observed between Pe $= 30-80$, due to the increasing buoyancy effects competing with flow convection forces. On the other hand, in Fig. 18 at the highest Rayleigh number investigated of Ra $= 2\times10^7$, the predictions show that the range of Péclet number without steady solutions increases in both the backward and forward directions. Hence, flow oscillation behaviour begins at Pe = 2 and vanishes at Pe = 340, extending the range of $15 \le$ Pe ≤ 190 at Ra $= 1\times10^7$, with a 1.93 times increase in Pe range. Furthermore, it is found in some cases, for example, at Pe = 40 and 50, chaotic flow behaviours develop in the channel.

In order to present a clearer picture between periodic, quasi-periodic, and chaotic flow behaviours generated in the channel at

(a) Variation of Nu_F with time at Ra=2×10^7 and Pe=100.

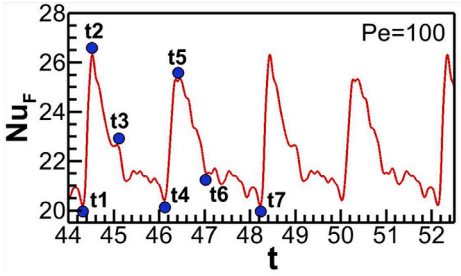

(b) Streamlines of flow.

Fig. 22. (a) Variations of Nu_F with time at $Ra = 2\times10^7$ and Pe = 100, and (b) streamlines of flow behaviour at different times indicated in (a).

Ra = 2×10^7, Figs. 19–23 display the transient flow field over each full oscillation period at different Péclet numbers Pe = 2, 4, 40, 100, 200, respectively. Fig. 19 shows the transient flow field under a weak forced flow in comparison to the buoyancy-induced flow. It is perhaps not surprising to see two pairs of recirculating cells generated in the flow domain, with the inner cells deformed and having a small aspect ratio of less than 0.3. It is obvious that this flow structure is a kind of unstable multicellular convection experiencing a full periodic oscillation with low frequency and small amplitude. As Péclet number increases to Pe = 4, it is shown in Fig. 20 that the inner cells are carried away by the forced flow, leaving a single pair of convective recirculating cells, which is also unstable. This pair of convective cells appear to have a nice quasi-periodic oscillation also with low frequency and small amplitude. However, as Péclet number is increased further to Pe = 40, the inner cells emerge again in the flow field. Nonetheless, they are shown to be in a destruction/regeneration repeating cycle, with the main external cells remaining but subject to high deformation. It can be seen that the flow field shows chaotic behaviour that commences with the destruction of the first internal cell followed by the second internal cell, then regeneration of both, and lastly with them combining. Very non-uniform flow behaviour is seen for this Péclet number. Interestingly, as the Péclet number is increased to Pe = 100, it can be seen that the flow field restores to a more quasi-periodic behaviour. This is possibly due to that increased strength of the forced flow, which restrains the instability of convective cells, but also increases their recirculation intensity. On increasing Péclet number further, the flow field returns to its usual periodic flow state at Pe = 200.

In this mixed convection regime, it is of particular interest to probe the impacts of Péclet and Rayleigh number on the temperature distributions of the flowing fluid and the solid particles that represent the two phases of the porous medium used. Figs. 24 and 25 present these distributions for the solid and fluid phases, as well as the localised temperature disparity between them ($T_f - T_s$), at different Péclet and Rayleigh numbers. It is shown in both figures that the solid thermal field is hardly affected by Péclet and Rayleigh numbers; however, these parameters considerably affect the fluid thermal field. Accordingly, one can see that the two phases tend to have similar thermal fields at low Péclet and/or Rayleigh numbers. This means that they are in local thermal equilibrium (LTE). However, as any one of these parameters increases, the disparity between temperature fields of the phases increases, indicating the loss of local thermal equilibrium condition between them. The hypothesis of local thermal equilibrium

(a) Variation of Nu_F with time at Ra=2×10^7 and Pe=200.

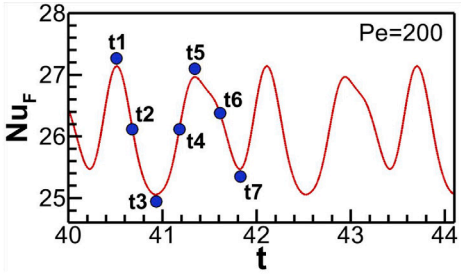

(b) Streamlines of flow.

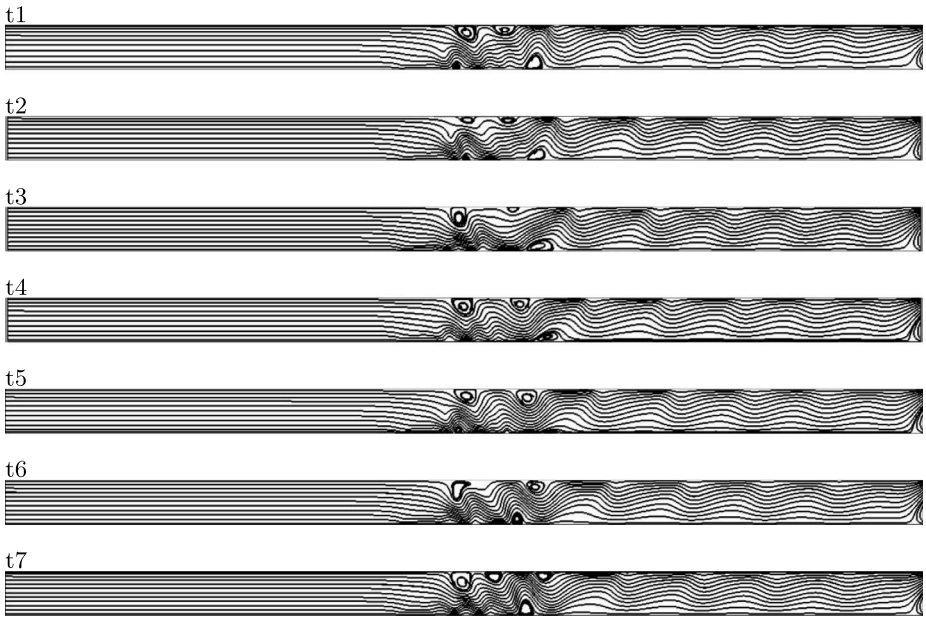

Fig. 23. (a) Variations of Nu_F with time at at Ra = 2×10^7 and Pe = 200, and (b) streamlines of flow behaviour at different times indicated in (a).

LTE when analysing convection heat transfer in porous media is well-described in Gazy et al. [39], defining the circumstances that make such hypothesis to be valid or not. For more insight, Fig. 26 shows the alteration of the average temperature discrepancy between both phases, $(\overline{T_f - T_s})$, against Péclet number for a range of Rayleigh numbers. The figure demonstrates that for low and moderate Péclet numbers Pe = 0.01–100, $(\overline{T_f - T_s})$ reduces as Rayleigh number decreases, but there is little effect of Péclet number. However, for high Pe ≥ 100, $(\overline{T_f - T_s})$ is increased significantly at increasing Péclet number, and the effect of Rayleigh number effectively vanishes.

6. Conclusions

In the current study, computational results are presented for unsteady mixed convection water flows and heat transfer within a horizontal plane channel packed with stainless steel beads, and heated from below with a localised heat source. The conclusions of this study are as follows.

(1) Generally, for small Péclet numbers, steady free convection dominates, while for high Péclet numbers, steady forced convection dominates. No oscillatory flows are found to develop in these free and forced convection regimes. However, interestingly, for moderate Péclet numbers, oscillatory mixed convective periodic flows develop. In some cases, quasi-periodic and chaotic flow behaviours are observed.

(2) For low Rayleigh numbers, Ra = 10^5 and 10^6, all the flow cases are steady; however, for high Rayleigh numbers, Ra ≥ 2×10^6, there always appears to be a critical Péclet number where Nusselt number has a minimal value, corresponding to the occurrence of oscillatory flow.

(3) At Ra = 2×10^6, the flow field becomes unstable for a certain range of Péclet number $5 \le Pe \le 20$, and this range increases as Rayleigh number increases.

(4) For low to moderate Péclet number Pe = 0.01–100, the average difference between the fluid and solid temperatures $(\overline{T_f - T_s})$ reduces as Rayleigh number is decreased, but without any influence from Péclet number. However, for high Pe ≥ 100, $(\overline{T_f - T_s})$ is increased significantly by increasing the Péclet number, while the impact of Rayleigh number vanishes.

7. Limitations of the present work

The current numerical code has the ability to solve the $2D$ problem, and consider the packed beads as circles. Indeed, the effort is directed to develop the numerical algorithm to solve the problem in $3D$ dimensions, dealing with the particles as spheres, to investigate the impacts of their parameters such as the particle diameter and porosity on the flow stability inside the $3D$ channel.

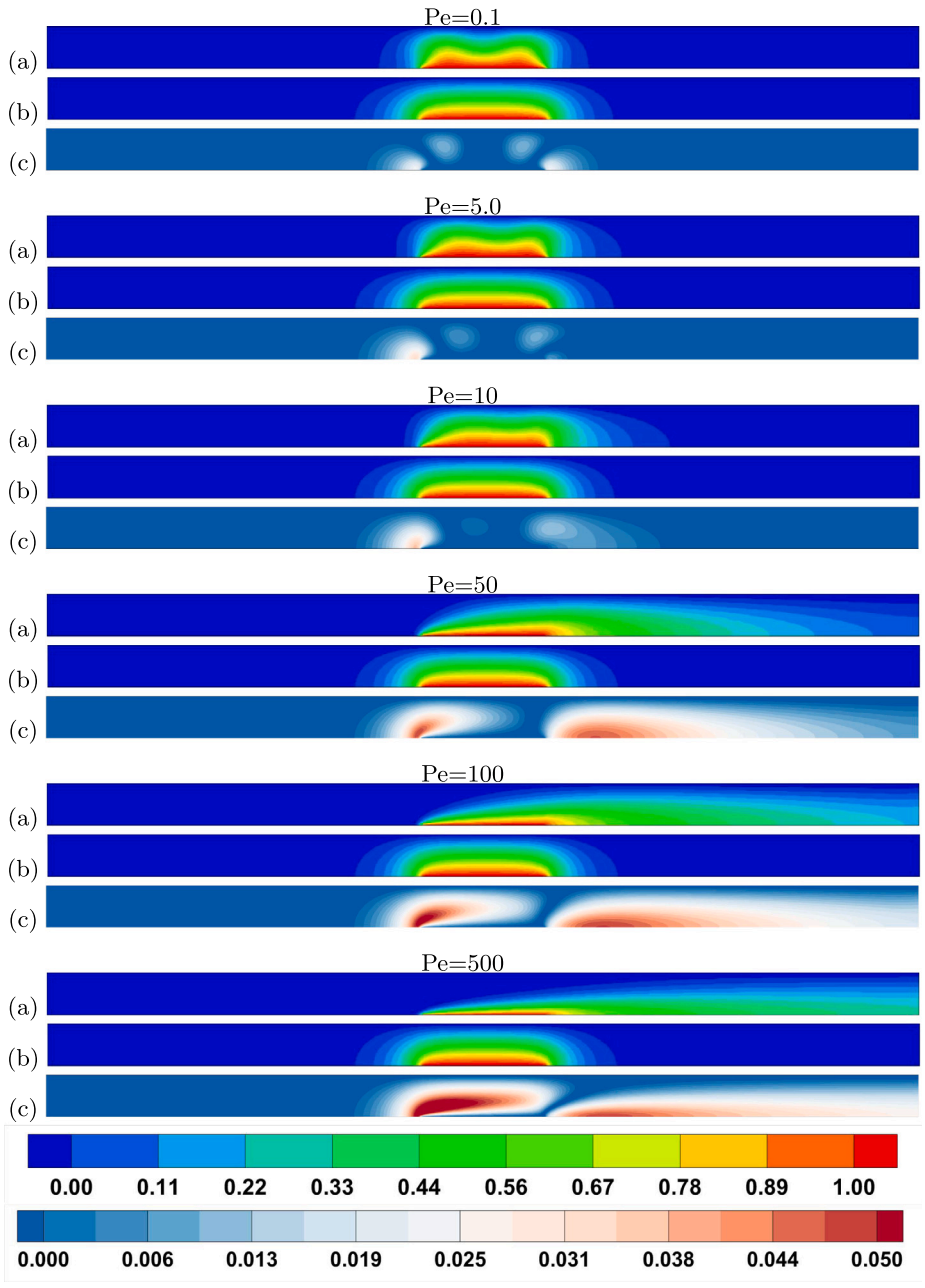

Fig. 24. (a) Fluid isotherms patterns, (b) Solid isotherms patterns, (c) $(T_f - T_s)$ between two phases, for different Péclet numbers at Ra $= 1 \times 10^6$.

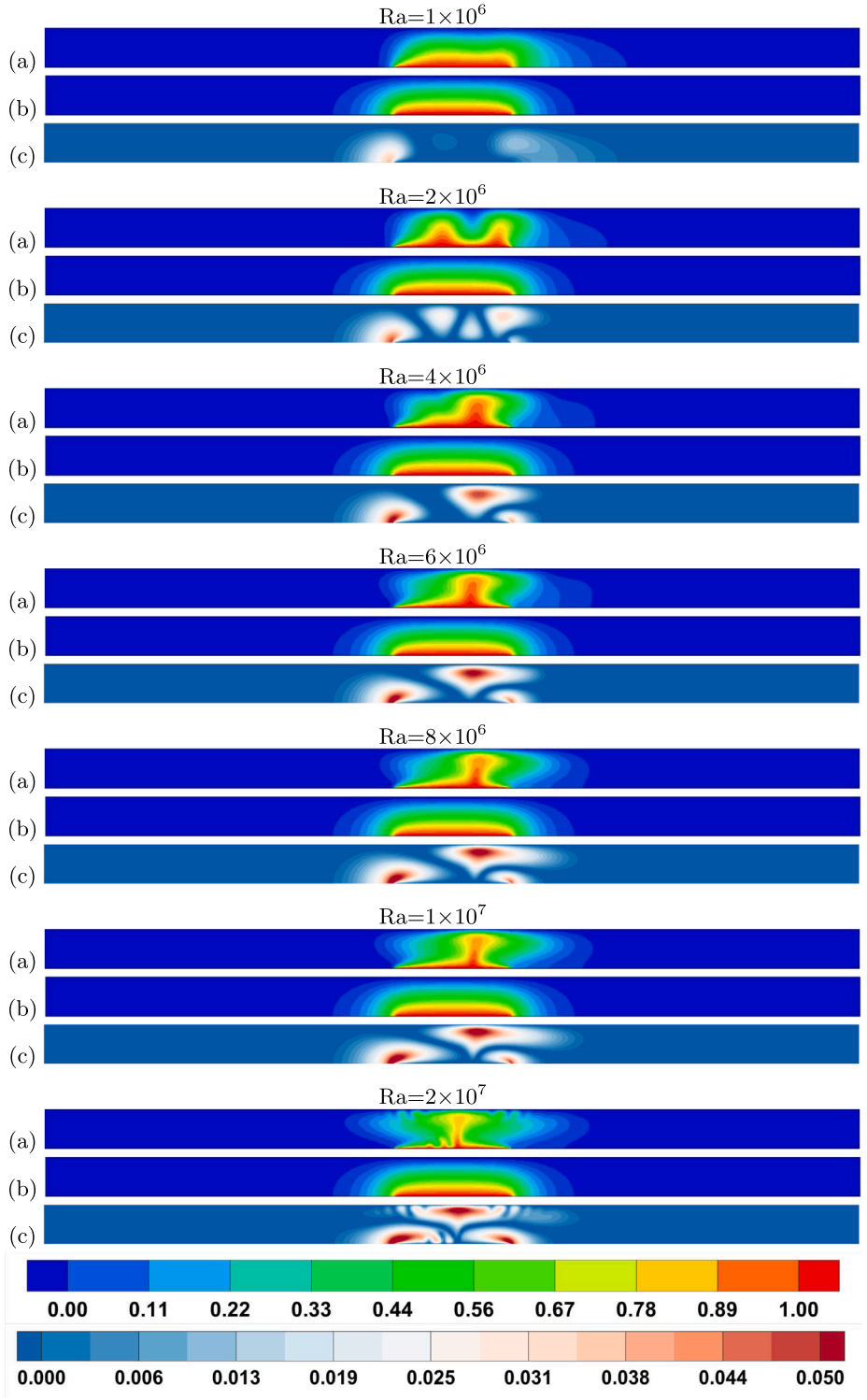

Fig. 25. (a) Fluid isotherms patterns, (b) Solid isotherms patterns, (c) $(T_f - T_s)$ between two phases, for different Rayleigh numbers at Pe = 10.

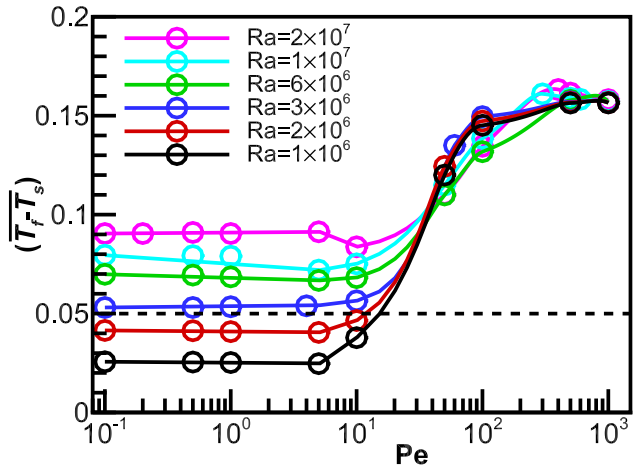

Fig. 26. Variations of average temperature difference ($\overline{T_f - T_s}$) with Pe for different Ra.

Nomenclature

a_{sf}	inter-phase surface area.
Bi	Biot number.
C_F	inertia factor.
c_p	parameter of specific heat.
d	diameter of spherical particles.
Da	Darcy number.
g	gravity.
H	height of channel.
h_{sf}	inter-phase convective coefficient.
k	thermal conductivity.
K	permeability.
L	length of channel.
L_s	length of heating element.
Nu_F	average fluid Nusselt number.
P	grid node.
P_f	pressure.
Pe	Péclet number.
Pr	Prandtl number.
Ra	Rayleigh number.
Re	Reynolds number.
T	temperature.
t	time.
u, v	velocities.
x, y	coordinates.

Greek symbols

α	thermal diffusivity.
β	volumetric expansion factor.
ρ	density.
ε	porosity.
μ	dynamic viscosity.
ν	kinematic viscosity.

Superscripts

~	dimensional quantity.

Subscripts

d	dispersive.
eff	effective.
f	fluid.
h	hot.
o	inlet.
p	particle level.
s	solid.
st	stagnant.

CRediT authorship contribution statement

Gazy F. Al-Sumaily: Conceptualization, Investigation, Methodology, Visualization. **Hasanen M. Hussen:** Writing – original draft, Writing – review & editing. **Hayder A. Dhahad:** Project administration, Resources. **Mark C. Thompson:** Software, Supervision, Validation. **Talal Yusaf:** Data curation, Formal analysis.

Declaration of competing interest

We wish to confirm that there are no known conflicts of interest associated with this publication and there has been no significant financial support for this work that could have influenced its outcome.

We confirm that the manuscript has been read and approved by all named authors and that there are no other persons who satisfied the criteria for authorship but are not listed. We further confirm that the order of authors listed in the manuscript has been approved by all of us.

We confirm that we have given due consideration to the protection of intellectual property associated with this work and that there are no impediments to publication, including the timing of publication, with respect to intellectual property. In so doing we confirm that we have followed the regulations of our institutions concerning intellectual property.

Data availability

Data will be made available on request.

Acknowledgements

This research was supported in part by the Monash eResearch Centre and eSolutions-Research Support Services through the use of the MonARCH HPC Cluster.

Funding

This research did not receive any specific grant from funding agencies in the public, commercial, or not-for-profit sectors.

References

[1] F.A. Gazy, A.D. Hayder, C.T. Mark, Mixed convection phenomenon in packed beds: A comprehensive review, TSEP 32 (2022) 101242.
[2] H. Hadim, G. Chen, Non-darcy mixed convection in a vertical porous channel with asymmetric wall heating, J. Thermophys. Heat Trans. 8 (4) (1994) 805–808.
[3] Y.C. Chen, J.N. Chung, C.S. Wu, Y.F. Lue, Non-Darcy mixed convection in a vertical channel filled with a porous medium, Int. J. Heat Mass Transfer 43 (13) (2000) 2421–2429.
[4] Y.J. Rami, A.B. Fawzi, A. Fahmi, Darcy-Forchheimer mixed convection heat and mass transfer in fluid saturated porous media, Int. J. Numer. Methods Heat Fluid Flow 11 (5/6) (2001) 600–618.
[5] G. Degan, P. Vasseur, Aiding mixed convection through a vertical anisotropic porous channel with oblique principal axes, Internat. J. Engrg. Sci. 40 (2) (2002) 193–209.
[6] I. Pop, D.A.S. Rees, C. Egbers, Mixed convection flow in a narrow vertical duct filled with a porous medium, Int. J. Therm. Sci. 43 (5) (2004) 489–498.
[7] J.C. Umavathi, J.P. Kumar, A.J. Chamkha, I. Pop, Mixed convection in a vertical porous channel, Transp. Porous Media 61 (3) (2005) 315–335.
[8] B. Buonomo, O. Manca, P. Mesolella, S. Nardini, Local thermal non-equilibrium in mixed convection in channels partially heated at uniform heat flux filled with a porous medium, in: Proceedings of the ASME 12th Biennial Conference on Engineering Systems Design and Analysis ESDA2014, Vol. 3, Copenhagen, Denmark, 2014, ESDA2014–20538.
[9] A.A. Avramenko, Y.Y. Kovetska, I.V. Shevchuk, A.I. Tyrinov, V.I. Shevchuk, Mixed convection in vertical flat and circular porous micro-channels, Transp. Porous Media 124 (2018) 919–941.
[10] K.C. Wong, N.H. Saeid, Numerical study of mixed convection on jet impingement cooling in a horizontal porous layer under local thermal non-equilibrium conditions, Int. J. Therm. Sci. 48 (5) (2009) 860–870.

[11] S.M. Aminossadati, B. Ghasemib, A numerical study of mixed convection in a horizontal channel with a discrete heat source in an open cavity, Eur. J. Mech. B Fluids 28 (2009) 590–598.
[12] F. Selimefendigil, Numerical analysis and POD based Interpolation of mixed convection heat transfer in horizontal channel with cavity heated from below, Eng. Appl. Comput. Fluid Mech. 7 (2) (2013) 261–271.
[13] F.C. Lai, V. Prasad, F.A. Kulacki, Effects of the size of heat source on mixed convection in horizontal porous layers heated from below, in: Proceedings of the 2nd ASME-JSME Thermal Engineering Joint Conference, Vol. 2, American Society of Mechanical Engineers, Honolulu, Hi, USA, 1987, pp. 413–419.
[14] V. Prasad, F.C. Lai, F.A. Kulacki, Mixed convection in horizontal porous layers heated from below, Trans. ASME, J. Heat Transfer 110 (2) (1988) 395–402.
[15] F.C. Lai, F.A. Kulacki, Transient mixed convection in horizontal porous layers locally heated from below, in: ASME Proceedings of the 1988 National Heat Transfer Conference, Vol. 96, Houston, TX, USA, 1988, pp. 353–364.
[16] F.C. Chou, P.Y. Chung, Effect of stagnant conductivity on non-Darcian mixed convection in horizontal square packed channels, Numer. Heat Transf. A 27 (2) (1995) 195–209.
[17] Y. Yokoyama, F.A. Kulacki, R.L. Mahajan, Mixed convection in a horizontal porous duct with a sudden expansion and local heating from below, Trans. ASME, J. Heat Transfer 121 (3) (1999) 653–661.
[18] P.Y. Chang, S.W. Shiah, M.N. Fu, Mixed convection in a horizontal square packed-sphere channel under axially uniform heating peripherally uniform wall temperature, Numer. Heat Transf. A 45 (8) (2004) 791–809.
[19] D. Cimpean, I. Pop, D.B. Ingham, J.H. Merkin, Fully developed mixed convection flow between inclined parallel plates filled with a porous medium, Transp. Porous. Media 77 (2009) 87–102.
[20] N.H. Saeid, I. Pop, Periodic mixed convection in horizontal porous layer heated from below by isoflux heater, Arab. J. Sci. Eng. Arab. J. Sci. Eng. 31 (2B) (2006) 153–164.
[21] K.C. Wong, N.H. Saeid, Numerical study of non-Darcian effects on jet impingement cooling in a horizontal porous layer in the mixed convection regime, Int. Commun. Heat Mass Transfer 36 (1) (2009) 45–50.
[22] J.M. Dixon, F.A. Kulacki, Mixed convection in fluid-superposed porous layers. Part 2: Experiments, Int. J. Heat Mass Transfer 109 (2017) 1301–1306.
[23] J.M. Dixon, F.A. Kulacki, Mixed convection in fluid superposed porous layers. Part 1: Analysis, Int. J. Heat Mass Transfer 109 (2017) 1289–1300.
[24] F. Ozgen, V. Yasin, Numerical study of mixed convection in a channel filled with a porous medium, Appl. Sci. 9 (2) (2019) 211–223.
[25] M. Kaviany, Principles of Heat Transfer in Porous Media, Springer-Verlag, 1995.
[26] D.A. Nield, A. Bejan, Convection in Porous Media, Third Edition, Springer Science+Business Media, New York, NY, USA, 2006.
[27] S.A. Mohammed, G.F. Al-sumaily, H.A. Dhahad, M.C. Thompson, Heat transfer enhancement with pressure drop optimisation in a horizontal porous channel locally heated from below, TSEP 26 (2021) 101013.
[28] S. Ergun, Fluid flow through packed columns, Chem. Eng. Progr. 48 (2) (1952) 89–94.
[29] F.A. Dullien, Media Fluid Transport and Pore Structure, Academic Press, New York, 1979.
[30] N. Wakao, S. Kaguei, T. Funazkri, Effect of fluid dispersion coefficients on particle-to-fluid heat transfer coefficients in packed beds- correlation of Nusselt numbers, Chem. Eng. Sci. 34 (3) (1979) 325–336.
[31] P. Zehner, E.U. Schluender, Thermal conductivity of granular materials at moderate temperatures, Chemie-Ingenieur-Technik 42 (14) (1970) 933–941.
[32] N. Wakao, S. Kaguei, Heat and Mass Transfer in Packed Beds, Gordon and Breach, New York, 1982.
[33] S.V. Patankar, Numerical Heat Transfer and Fluid Flow, Hemisphere Publishing Corporation, New York, 1980.
[34] J.H. Ferziger, M. Peric, Computational Methods for Fluid Dynamics, Springer, Berlin, 1997.
[35] W.H. Alawee, G.F. Al-sumaily, H.A. Dhahad, M.C. Thompson, Numerical analysis of non-Darcian mixed convection flows in a ventilated enclosure filled with a fluid-saturated porous medium, TSEP 24 (2021) 100922.
[36] A.D. Hayder, F.A. Gazy, H.A. Wissam, C.T. Mark, Aiding and opposing re-circulating mixed convection flows in a square vented enclosure, TSEP 19 (2020) 100577.
[37] R.N. Horne, M.J. O'Sullivan, Oscillatory convection in a porous medium heated from below, J. Fluid Mech. 66 (1974) 339–352.
[38] R.N. Horne, M.J. O'Sullivan, Origin of oscillatory convection in a porous medium heated from below, Phys. Fluids 21 (1978) 1260–1264.
[39] F.A. Gazy, A. Amged, A.D. Hayder, C.T. Mark, Y. Talal, Legitimacy of the local thermal equilibrium hypothesis in porous media: A comprehensive review, Energies 14 (2021) 8114.